A Theoretical Analysis of Vacuum Arc Thruster Performance *

James E. Polk, Mike Sekerak and John K. Ziemer
Jet Propulsion Laboratory, M/S 125-109, 4800 Oak Grove Drive, Pasadena, CA 91109
(818) 354-9275, james.e.polk@jpl.nasa.gov

Jochen Schein, Niansheng Qi and Robert Binder
Alameda Applied Sciences Corp, 2235 Polvorosa Ave, San Leandro, CA 94577
(510) 483-4156, schein@aasc.net

André Anders
Lawrence Berkeley National Laboratory, 1 Cyclotron Road, Berkeley, CA 94720
(510) 486-6745, aanders@lbl.gov

IEPC-01-211[†]

In vacuum arc discharges the current is conducted through vapor evaporated from the cathode surface. In these devices very dense, highly ionized plasmas can be created from any metallic or conducting solid used as the cathode. This paper describes theoretical models of performance for several thruster configurations which use vacuum arc plasma sources. This analysis suggests that thrusters using vacuum arc sources can be operated efficiently with a range of propellant options that gives great flexibility in specific impulse. In addition, the efficiency of plasma production in these devices appears to be largely independent of scale because the metal vapor is ionized within a few microns of the cathode electron emission sites, so this approach is well-suited for micropropulsion.

Introduction

Vacuum arcs, or discharges burning in metal vapor liberated from the cathode into an interelectrode gap initially at vacuum, produce high velocity, highly ionized plasma flows which can be exploited for propulsion applications. On cathode surfaces which are too cold to support bulk thermionic emission, current continuity across the metal-vacuum interface is maintained through one or more highly mobile, luminous spots. Although the bulk cathode temperature is relatively low, the local temperature in these spots is well over the boiling point of the cathode material and electrons are emitted by a combination of thermal and field emission. These emission sites are initiated at locations where there are local micro-protrusions or dielectric inclusions which cause local enhancement of the applied electric field. Field emission in these regions causes explosive vaporization of the microprotrusion or inclusion due to very rapid Joule heating. A combination of Joule heating and ion bombardment heating sustains the temperatures required to emit electrons and vaporize cathode material. The loss of cathode material causes the formation of a tiny crater on the surface. As the crater diameter grows, the power deposition by ohmic heating and ion bombardment decreases. Eventually the temperature drops to the point where it is no longer possible to sustain electron and vapor emission and the site extinguishes. The characteristic site lifetime appears to be on the order of a few tens of nanoseconds [?]. The resulting craters have a diameter that is typically only 1-10 microns [?], although gross melting may result in larger structures [?]. The extinction of an emission site is generally followed by the igni-

tion of a new site at a nearby microprotrusion, often apparently self-generated by the molten metal flows from the previous site. The luminous spot therefore appears to move over the cathode surface.

Extraordinary conditions are achieved in the cathode spots. Current densities on the order of 10^8 A/cm^2 [?] in the emission site and heat fluxes of 10^8–10^9 W/cm^2 [?] produce rapid vaporization and ionization of the cathode material. Plasma densities in the near-cathode region reach 10^{20}–10^{21} cm^{-3} [?], nearly the density of the solid metal. The plasma is generally almost 100 percent ionized, often with multiple charge states [?]. What is truly remarkable is how easy it is to generate these conditions in cold cathode arc discharges. These extreme environments lead to vigorous acceleration of the metal vapor plasma away from the cathode spot, and velocities achieved in the expanding plasma plume are typically on the order of 10^4 m/s [?].

Vacuum arc-generated plasmas can be used in several different types of propulsion devices. The plasma plumes produced in cathode spots are highly directional, and can be used to produce thrust directly. Vacuum arcs may also be used as plasma sources in ion accelerators such as ion or Hall thrusters. The focus of this paper is on application of vacuum arc discharges in thermal Vacuum Arc Thrusters (VAT's) and in electrostatic Vacuum Arc Ion Thrusters (VAIT's). The unique physical conditions achieved in vacuum arcs offer several potential advantages in these devices. A highly ionized plasma is generated very efficiently in cathode spot operation. Because the ionization process occurs within tens of microns of the emission site, the plasma source is inherently scalable to very small sizes for micropropulsion applications. No magnetic field is required for an efficient discharge, as in electron bombardment ion engines. Vacuum arc discharges can be operated in pulses with no sacrifice in plasma production efficiency, so the duty cycle can be varied to match the engine power to that available from the spacecraft. This can enable the use of high specific impulse electric thrusters for power-constrained microspacecraft. Finally, because the propellant is provided by the consumable cathode, no gas feed system is necessary. This not only reduces mass and volume, but

eliminates the need for low leak-rate valves. It is very difficult to achieve low leak rates in microfabricated valves, so this is a significant advantage over conventional ion engines for microspacecraft applications.

Vacuum arc discharges exhibit certain regularities in their behavior which allow simple, semi-empirical models of thruster performance. The purpose of the models developed in this paper is to provide guidance in choosing cathode materials and explore the performance potential of several implementations of vacuum arc thrusters. We will first describe the performance models and then discuss the performance characteristics of a number of candidate propellants.

A Semi-Empirical Performance Model

Vacuum Arc Plasma Sources

Mass is eroded from cathode spots in the form of metal vapor ions, droplets or "macroparticles," and neutral vapor [?], although the majority of the neutral vapor appears to be evaporated from the macroparticles in flight [?]. For sufficiently low values of energy deposited in the cathode (low average current density and/or short pulses), the total erosion rate $\dot{m}_t$ scales with the arc discharge current J_d [?],

$$\dot{m}_t = E_r J_d, \qquad (1)$$

The erosion rate E_r is constant in this regime because the mass loss occurs primarily within single, isolated emission sites. Higher current levels are accommodated by more emission sites. Above a certain threshold current or during long pulses the temperature fields of individual emission sites may overlap and cause gross melting. Under these conditions the droplet erosion rate may increase dramatically [?].

The ion component of the mass flux can be described as an ion current J_i, which is the sum of the currents J_Z associated with the fluxes of ions in various charge states Z. Experiments over a wide range of conditions show that the ion current in the spot plasma plume can be expressed as a nearly constant fraction f_i of the discharge current ranging from 0.07 to 0.1 [?]. We can therefore write the ion flow in the cathode spot plasma as

$$J_i = \sum_Z J_Z = f_i J_d \qquad (2)$$

and the ion mass flow rate as

$$\dot{m}_i = \sum_Z \frac{J_Z M_i}{Ze} = \frac{f_i J_d M_i}{e}\langle Z^{-1}\rangle, \qquad (3)$$

where e is the charge on an electron, M_i is the mass of the ion, $\langle Z^{-1}\rangle$ represents the mean inverse charge state,

$$\langle Z^{-1}\rangle = \sum_Z \frac{f_Z}{Z}. \qquad (4)$$

and f_Z is the ratio of the current due to a single charge state to the total ion current,

$$f_Z = \frac{J_Z}{J_i}. \qquad (5)$$

This charge state distribution is assumed to be constant for a given cathode material. An equilibrium composition of multiply charged ions is created in the hot, high density metal vapor plasma near the emission zone and "freezes" at some point in the plume from the cathode spot as the recombination rate drops due to plasma expansion and cooling. Measurements in pulsed discharges show that the charge state distribution for a certain material changes over the first 100 μs of the discharge and then becomes relatively constant [?]. The charge state distribution does not vary significantly with discharge current over a range of 50-400 A [?], but may be influenced by applied magnetic fields [?] and higher discharge currents [?]. The fraction of the total mass loss that occurs in the form of ions is given by the expression

$$F_i = \frac{f_i M_i \langle Z^{-1}\rangle}{e E_r}. \qquad (6)$$

The plasma is accelerated to high velocities within a few hundred microns of the cathode spot by gasdynamic (electron pressure gradient and electron-ion friction) forces and possibly by electrostatic forces created by a potential hump that forms above the emission site [?]. Experimental measurements of the ion current density in the plume expanding from the cathode region in vacuum arcs suggest that it follows a cosine [?] or exponential distribution [?]. The geometry used in defining these distributions is shown in Fig. (1). For a cosine distribution in polar coordinates the current density at a radius l and angle ϕ
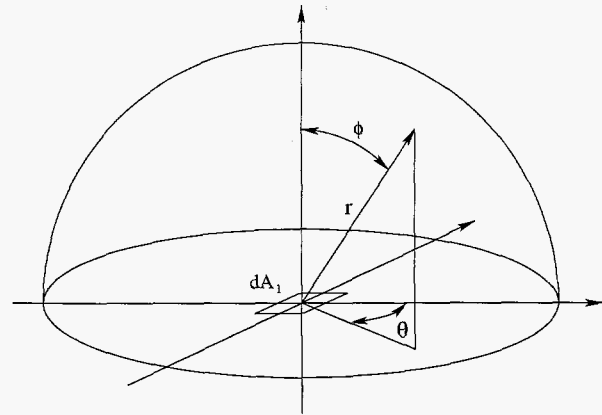

Figure 1: Geometry used to define ion current distribution.
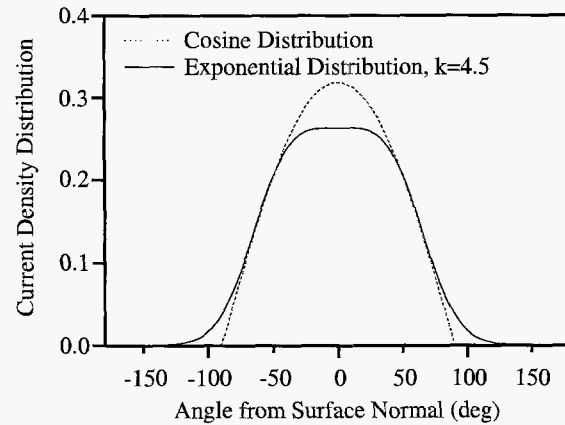

Figure 2: Normalized angular ion current distribution for cosine and exponential functions.

defined from the surface normal due to mass generated in area dA_1 on the cathode surface is

$$j_{ip}(l,\phi) = \frac{j_{ic}\cos\phi dA_1}{\pi l^2} \qquad (7)$$

where j_{ic} is the ion current flux from the cathode surface. This function normalized to a value of $j_{ic}dA_1 = 1$ is plotted in Fig. (2).

The cosine distribution is naturally truncated at $\phi = 90$ degrees, but ion current is often observed at higher angles [?]. This ion backflow is obviously not generated at the cathode surface but is the result of forces acting on the plasma plume away from the electrode structure. The exponential distribution assumes that the current drops exponentially with the solid angle subtended by the polar angle ϕ. This distribution often more accurately captures the ion cur-

rent density at high angles, and as shown in Fig. (2), permits ion current backflow. This distribution is given by

$$j_{ip}(l, \phi) = \frac{2j_{ic}dA_1}{\sqrt{\pi}l^2 k \operatorname{erf}(2\pi/k)} \times \exp(-[2\pi(1 - \cos\phi)]^2/k^2), \quad (8)$$

where k is a constant which determines the spread in the distribution. With the assumptions discussed above, the ion current density at the cathode surface can be written as $j_{ic} = f_i j_d$. The ion mass flow rate at the point (l, ϕ) due to erosion at dA_1 is given by

$$\dot{m}_{ip}(l, \phi) = \frac{M_i j_{ip}}{e} \langle Z^{-1} \rangle. \quad (9)$$

This relationship relies on the assumption that the charge state distribution is independent of angle, so that $j_Z/j_{ip} = f_Z$ everywhere in the plume. Some angular variation in charge state distribution due to electric fields in the plume and charge exchange with neutral atoms evaporated from macroparticles at high angles is calculated theoretically [?] or observed in experiments [?]. These effects are not expected to significantly affect the calculated performance, however.

The ion velocity u_i is assumed to be a constant for all ion charge states of a given material. This is justified by experimental data which generally show that the velocity does not vary significantly with current or angle [?]. A weak variation with charge state is observed, apparently due to XXX [?]. The discharge voltage V_d is also assumed to be constant for a given cathode material. This is also justified by experiment, which shows that the burning voltage for a given material is dominated by the cathode fall [?]. The voltage does vary weakly with anode geometry [?] and significant voltage drops can occur in current leads or the cathode material itself [?].

Vacuum Arc Thruster Performance

In the vacuum arc thruster (VAT) the expanding cathode spot plasma is used to produce thrust. The general configuration of a thruster developed by Alameda Applied Sciences Corporation [?] is shown in Fig. (3). Figure (4) shows a photograph of a VAT with a titanium cathode and molybdenum anode that was built and tested at JPL. This design consists of a
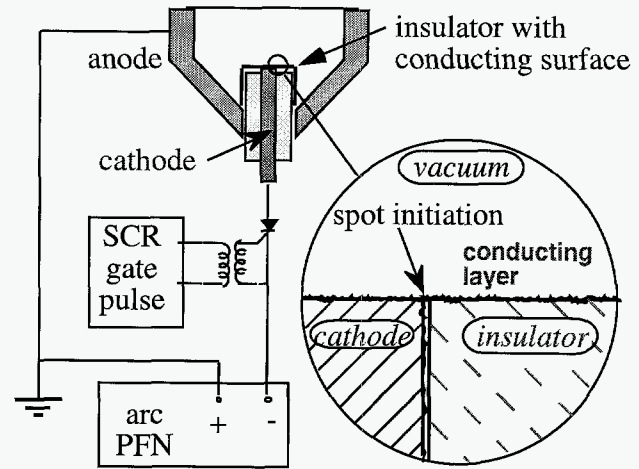

Figure 3: Schematic of a vacuum arc thruster.

Figure 4: Photograph of a laboratory model vacuum arc thruster.

central rod-shaped cathode separated from a coaxial anode by a thin-walled insulating tube. The face of the cathode and insulator may in general be recessed from the anode face. The consumable cathode rod would have to be fed into the discharge region as material is eroded from it. Inductively or capacitively driven pulsed discharges are ignited in this configuration by what is called"triggerless" operation [?]. A thin conducting film on the surface of the insulator produces a high but finite impedence between the cathode and anode. When a relatively low voltage of several hundred volts is applied between the electrodes breakdown occurs at very small gaps or flaws in the thin metal film. These tiny discharges produce enough metal vapor to initiate the main discharge in the gap. Metal vapor and droplets eroded from the cathode replenish the thin conducting layer on the insulator.

The thrust for this configuration can be derived by integrating the momentum flux through the aperture in the anode plane. The geometry used to calculate the thrust is shown in Fig. (5). The differential thrust due to ion flux from area dA_1 on the cathode surface through area dA_2 at the anode exit plane is
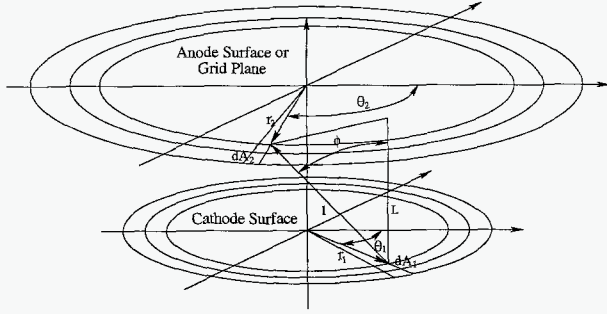
Figure 5: Geometry used to calculate the momentum flux through the anode plane.

given by

$$
\begin{aligned}
dT &= d\dot{m}_{ip}(l, \phi)(u_i \cos \phi)(\cos\phi dA_2) \\
&= \frac{M_i j_{ip}}{e}\langle Z^{-1}\rangle u_i \cos^2 \phi dA_2.
\end{aligned} \tag{10}
$$

Integrating this over the cathode surface and the anode exit plane yields the expression

$$
T = \frac{M_i f_i J_d u_i}{e}\langle Z^{-1}\rangle C_t(\overline{L}, \overline{r}_a), \tag{11}
$$

which represents the thrust that would be achieved if all of the eroded ion flux exited the engine with a velocity u_i directed along the axis multiplied by a thrust correction factor C_t which accounts for plume divergence and deposition of eroded cathode material on the anode interior walls. This expression also assumes that the discharge current density is uniform over the cathode surface, $j_d = J_d/\pi r_c^2$, where r_c is the cathode radius. In any single discharge this assumption is violated because the current is highly nonuniform, concentrated in individual cathode spots. This approach will give the correct average thrust over many discharges if the erosion rate of the cathode is uniform, as it must be in a good thruster design.

The thrust correction factor for a cosine distribution is given by integrating over the cathode source plane to determine the total momentum flux through a point on the anode exit plane and then integrating that result over the anode exit area. This yields

$$
C_t = \frac{\overline{L}^3}{\pi^2} \int_0^{2\pi}\!\!\int_0^{2\pi}\!\!\int_0^{\overline{r}_a}\!\!\int_0^1 \frac{\overline{r}_1 \overline{r}_2 d\overline{r}_1 d\overline{r}_2 d\theta_1 d\theta_2}{\overline{l}^5}, \tag{12}
$$

where $\overline{l} = [\overline{L}^2 + \overline{r}_1^2 + \overline{r}_2^2 - 2\overline{r}_1\overline{r}_2 \cos(\theta_1 - \theta_2)]^{1/2}$. The thruster geometry parameters are nondimensionalized by the cathode radius, so $\overline{L} = L/r_c$ where L is the cathode length, $\overline{r}_1 = r_1/r_c$ and $\overline{r}_2 = r_2/r_c$, where r_1 and r_2 are the radii in the cathode and anode planes and $\overline{r}_a = r_a/r_c$, where r_a is the anode exit radius. The angles in the cathode and anode planes are given by θ_1 and θ_2. The corresponding thrust correction factor for the exponential distribution is

$$
C_t = \frac{2\overline{L}^2}{\pi^{3/2}k \operatorname{erf}(2\pi/k)}I_1 \tag{13}
$$

where

$$
I_1 = \int_0^{2\pi}\!\!\int_0^{2\pi}\!\!\int_0^{\overline{r}_a}\!\!\int_0^1 \frac{\exp(\frac{-[2\pi(1-\overline{L}/\overline{l})]^2}{k^2})dA_1 dA_2}{\overline{l}^4} \tag{14}
$$

and $dA_1 dA_2 = \overline{r}_1\overline{r}_2 d\overline{r}_1 d\overline{r}_2 d\theta_1 d\theta_2$. These integrals were evaluated numerically for a range of electrode goemetry parameters $\overline{L}$ and $\overline{r}_a$ and plotted in Fig. (6). For the exponential distribution a spread factor $k = 4.5$ was chosen, based on measurements made with a copper vacuum arc discharge at 100 A [?]. The maximum thrust is achieved when the anode and cathode surfaces are coplanar, so the anode does not shadow the plasma flux. With this geometry, the thrust coefficient is 0.67 for a cosine distribution and 0.64 for an exponential distribution with $k = 4.5$. This maximum thrust coefficient represents the thrust loss due to plume divergence alone.

The specific impulse for a VAT is given by the expression

$$
\begin{aligned}
I_{sp} &= \frac{T}{\dot{m}_t g} = \frac{M_i f_i u_i C_t}{e E_r g}\langle Z^{-1}\rangle \\
&= \frac{F_i u_i C_t}{g}.
\end{aligned} \tag{15}
$$

The power consumed in this simple device is just the discharge power, $P = J_d V_d$. The total efficiency can therefore be expressed as

$$
\eta = \frac{T^2}{2\dot{m}_t P} = \frac{M_i^2 f_i^2 u_i^2 C_t^2(\langle Z^{-1}\rangle)^2}{2e^2 E_r V_d}, \tag{16}
$$

and the thrust-to-power ratio is

$$
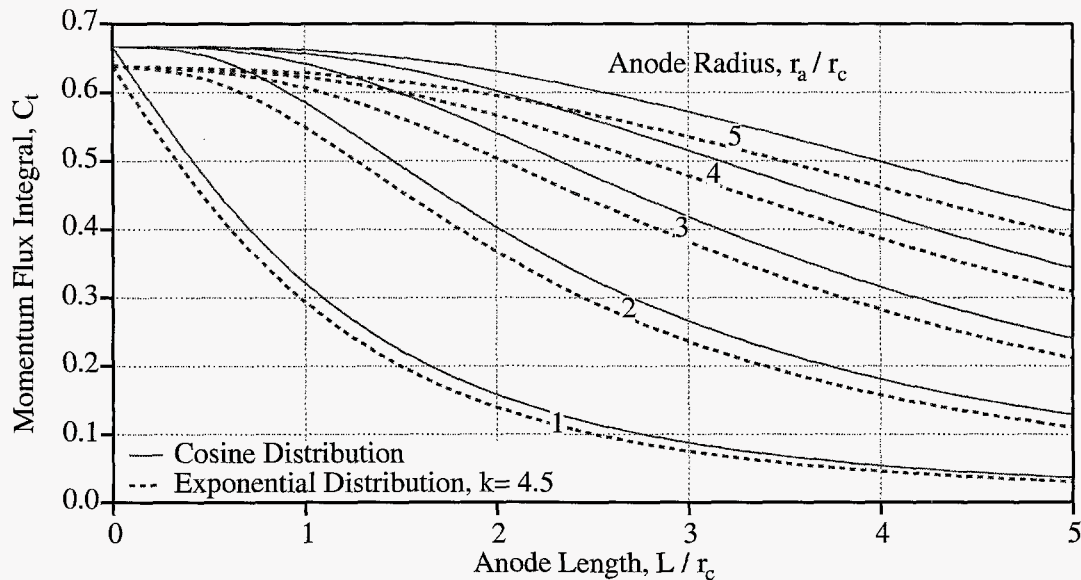T/P = \frac{M_i f_i u_i C_t}{e V_d}\langle Z^{-1}\rangle. \tag{17}
$$

Figure 6: Thrust factor which corrects for plume divergence and loss of plasma to anode walls.

The thrust of a VAT scales with the ion mass M_i, ion current fraction f_i, plasma velocity u_i and the charge state distribution factor $\langle Z^{-1} \rangle$, which are fundamentally cathode material properties. It also scales with the discharge current J_d, which is limited to values greater than the chopping current (the minimum value required to sustain a vacuum arc discharge) and less than the threshold for gross melting. The thrust also depends on the thrust coefficient C_t, which argues for an electrode geometry in which the anode does not intercept the cathode spot plasma, such as flush anode and cathode faces. However, other considerations may affect this conclusion. The discharge voltage will depend to some extent on electrode geometry and will likely be higher if the anode surface is not in good contact with the low impedance plasma. Because the droplet flux from the cathode is peaked at high angles (i.e. along the cathode surface) [?], most of the droplets will be captured on the interior anode wall in geometries with a recessed cathode. Some loss in thrust and efficiency may be tolerable if it results in less mass deposition on the spacecraft.

The specific impulse also depends on the material properties and the geometry, but varies inversely with the cathode erosion rate E_r. For a fixed ion current fraction f_i, a lower total erosion rate implies lower droplet erosion, a mass flux from the consumable cathode which does not contribute significantly to the thrust. The I_{sp} is independent of the discharge current because the plasma acceleration occurs in individual cathode spots for low currents. Increasing the discharge current changes the number of active emission sites, but does not influence the fundamental acceleration mechanism. At higher current levels interactions between spots may lead to additional electromagnetic or electrothermal acceleration, but this will likely occur under conditions which also lead to gross melting and intolerable droplet erosion. The total efficiency scales with the squares of the thrust parameters, inversely with erosion rate and discharge voltage and is independent of discharge current. This underscores the importance of designs which minimize voltage drops in the current leads, cathode structure and interelectrode plasma. For many power-limited micropropulsion applications the thrust-to-power ratio is a critical parameter. To maximize the T/P, cathode material with high values of the parameters M_i, f_i, u_i and low charge state distributions should be chosen and the electrode geometry should be designed to maximize the parameter C_t/V_d.

Vacuum Arc Ion Thruster Performance

In Vacuum Arc Ion Thrusters (VAIT's) a device like the VAT is used to supply a plasma which is
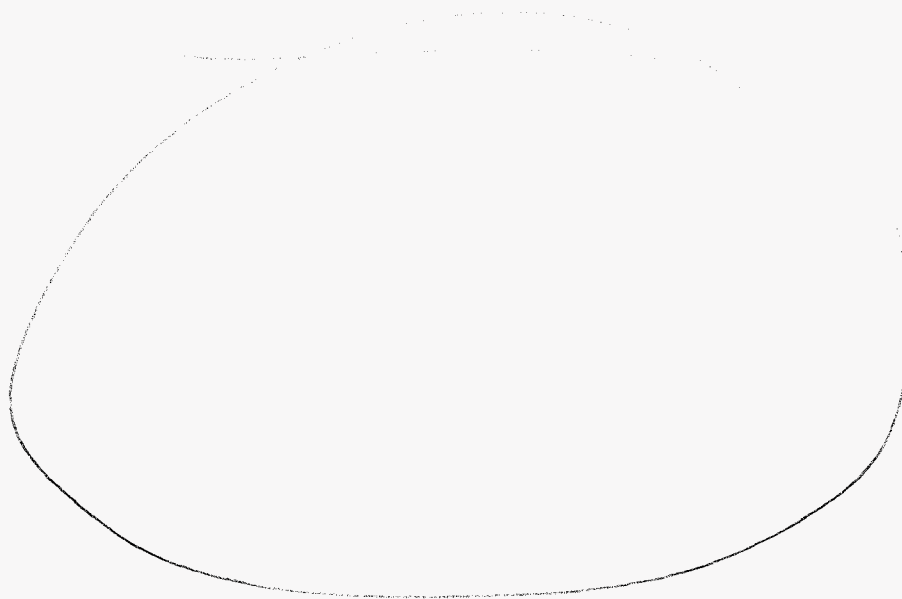
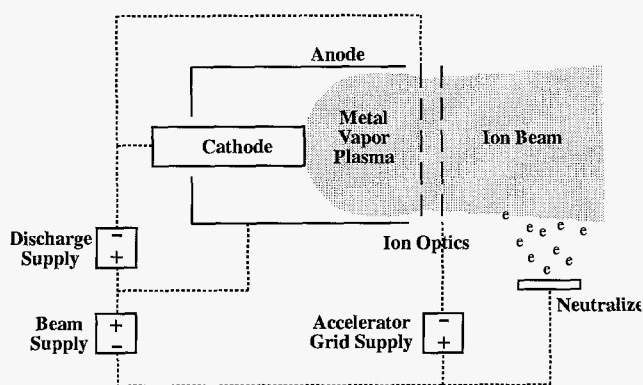Figure 8: Photograph of a laboratory model vacuum arc ion thruster.

Figure 7: Schematic of a vacuum arc ion thruster.

then accelerated electrostatically with ion optics. A schematic of this implementation with two grid ion optics is shown in Fig. (7), and Fig. (8) shows a photograph of a laboratory model thruster built by JPL and Alameda Applied Sciences Corporation. VAIT's are more complex than the VAT discussed above, but offer much higher performance potential because the ion acceleration process is decoupled from the plasma production.

The operation of the plasma source for the VAIT is assumed to be like that described by the model discussed above. The beam current is given by the fraction of the total arc ion current which is extracted by the ion optics,

$$J_b = f_i J_d C_j \phi_g. \tag{18}$$

The fraction of the total ion current $f_i J_d$ intercepted by the grids is given by the parameter C_j and the fraction of that accelerated through the ion optics is given by the grid transparency ϕ_g. The current fraction incident on the grids is determined by integrating the current flux from the cathode over the grid area, similar to the procedure used above to determine the momentum flux integral. For a cosine distribution this yields

$$C_j = \frac{\overline{L}^2}{\pi^2} \int_0^{2\pi}\!\!\int_0^{2\pi}\!\!\int_0^{\overline{r}_g}\!\!\int_0^1 \frac{\overline{r}_1 \overline{r}_2 d\overline{r}_1 d\overline{r}_2 d\theta_1 d\theta_2}{\overline{l}^4}. \tag{19}$$

For an exponential distribution the optics current is

$$C_j = \frac{2\overline{L}}{\pi^{3/2} k \, \mathrm{erf}(2\pi/k)} I_2 \tag{20}$$

where

$$I_2 = \int_0^{2\pi}\!\!\int_0^{2\pi}\!\!\int_0^{\overline{r}_g}\!\!\int_0^1 \frac{\exp\!\left(\frac{-[2\pi(1-\overline{L}/\overline{l})]^2}{k^2}\right) dA_1 dA_2}{\overline{l}^3}. \tag{21}$$

and, as above, $dA_1 dA_2 = \overline{r}_1 \overline{r}_2 d\overline{r}_1 d\overline{r}_2 d\theta_1 d\theta_2$. In these expressions, L is the distance between the cathode and the screen grid, $\overline{L} = L/r_c$, r_g is the radius of the ion optics active beam area and $\overline{r}_g =$
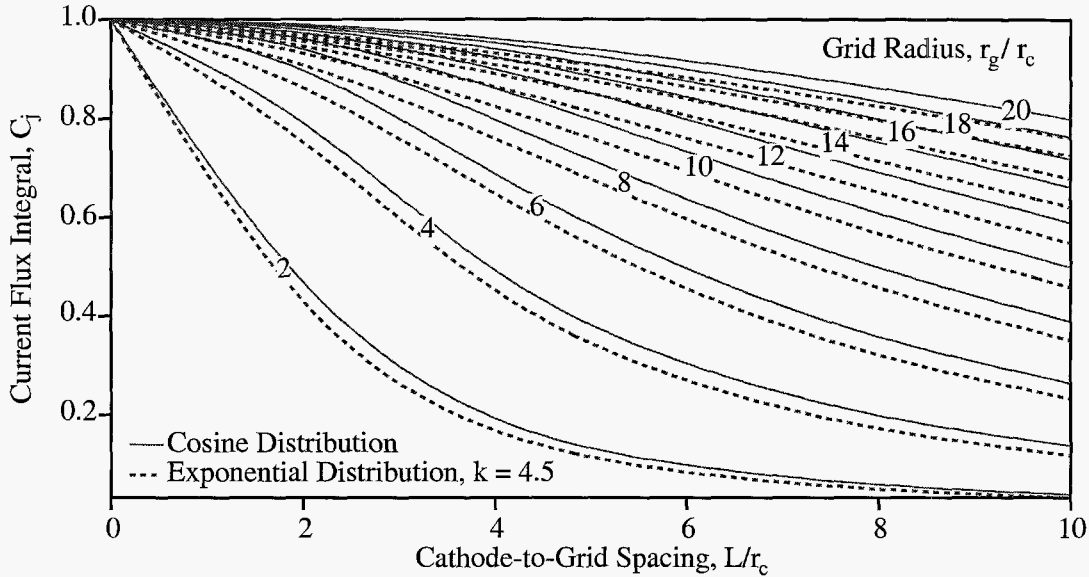
Figure 9: Geometry factor which accounts for ion current to surfaces other than the ion optics.

r_g/r_c. These integrals are plotted in Fig. (9) for a range of cathode-grid geometry parameters. As with the VAT, these relationships are not valid for a single discharge with a nonuniform distribution of current on the cathode surface, but yield the correct values averaged over many discharges if the cathode erodes uniformly. The grid transparency ϕ_g is assumed to be equal to the physical open area fraction of the screen grid. Ion optics with a quiescent upstream plasma typically exhibit an effective transparency greater than the open area fraction because the convex sheath upstream of the screen grid extracts ions from an area larger than the aperture area. In vacuum arc sources the plasma typically approaches the grid with a velocity greater than the Bohm velocity, so the ion trajectories will be less affected by the convex equipotential lines near the entrance to the screen grid aperture and the effective transparency will be close to the physical open area fraction.

Equation (18) assumes that the beam current extraction is not limited by optics focusing effects. If we model the ion optics as a plane diode, the maximum ion current density that can be extracted from the upstream plasma is given by the Child-Langmuir law [?],

$$j_b^{max} = \frac{4\epsilon_0}{9\langle Z^{-1/2}\rangle}\left(\frac{2e}{M_i}\right)^{1/2}\frac{V_t^{3/2}}{l_e^2}. \qquad (22)$$

In this expresssion, ϵ_0 is the permittivity of free space, l_e is the effective gap over which the ions are accelerated, $\langle Z^{-1/2}\rangle = \sum_Z f_Z/Z^{1/2}$, and the total accelerating voltage between the grids V_t is the difference between the beam voltage V_b and the accelerator grid voltage V_a. In reality, the current flow between the grids is always at the space charge limit; the plasma boundary (upstream sheath edge) moves, varying the effective acceleration length l_e, so that the beam current density given in Eq. (22) is consistent with the flux of ions toward the screen grid aperture. As the upstream plasma flux increases, the plasma boundary moves into the screen grid aperture, and at a certain value of the upstream density the sheath no longer properly focuses the ions through the accelerator grid aperture. This perveance limit for circular apertures is given approximately by Eq. (22) if $l_e = [l_g^2 + d_s^2/4]^{1/2}$, where l_g is the gap between the grids and d_s is the screen grid hole diameter [?]. For a VAIT, the peak ion current density at the screen grid must not exceed the value given by Eq. (22) to avoid direct ion impingement on the accelerator grid. This places a limit on the maximum discharge current (which controls the total plasma production rate and therefore the ion current density) that can be used for a given geometry.

The peak ion current density at the screen grid

depends on the distribution of discharge current on the cathode surface and the angular distribution of plasma flowing from the cathode spots. We will consider two limiting cases for each of the angular distributions considered above. The worst case condition occurs when the discharge current is below the spot-splitting current and a single cathode spot carries the entire discharge current. The peak ion current density then occurs directly above this spot. The other limiting case occurs when the discharge current is much higher than the spot splitting current and many spots are simultaneously active. In this limit the discharge current density is approximated as a uniform distribution over the entire cathode surface. The peak ion current density at the screen grid will then occur along the centerline of the thruster. In all cases the peak ion current density at the screen grid is given by an expression of the form,

$$j_{ip}^{max} = \frac{f_i J_d C_j^*(\overline{L})}{\pi r_c^2} \tag{23}$$

where C_j^* is a geometry factor which depends on $\overline{L}$, the ratio of the distance between the cathode and the grids and the cathode radius.

For a cosine ion current density distribution the geometry parameter for operation with a single spot (low discharge currents) is

$$C_j^* = \frac{1}{\overline{L}^2}. \tag{24}$$

For operation with many cathode spots (high discharge currents), the peak ion current density at the grids scales with the factor

$$C_j^* = \frac{1}{\overline{L}^2 + 1}. \tag{25}$$

For an exponential distribution, single spot operation yields a peak ion current density geometry parameter of

$$C_j^* = \frac{2\sqrt{\pi}}{\overline{L}^2 k \, \text{erf}(2\pi/k)}. \tag{26}$$

For multiple spot operation, the peak ion current density scales with

$$C_j^* = \frac{4\sqrt{\pi}\,\overline{L}}{k \, \text{erf}(2\pi/k)} \times \int_0^1 \frac{\exp(\frac{-[2\pi(1-\overline{L}/\overline{l})]^2}{k^2})\overline{r}_1 d\overline{r}_1}{\overline{l}^{3/2}}. \tag{27}$$

Equating these expressions to the space charge-limited current density defined by Eq. (22) and solving for J_d gives expressions for the maximum discharge current,

$$J_d^{max} = \frac{4\pi r_c^2 \epsilon_0}{9 f_i C_j^* \langle Z^{-1/2} \rangle} \left(\frac{2e}{M_i}\right)^{1/2} \frac{V_t^{3/2}}{l_e^2}. \tag{28}$$

It may be possible to extract more beam current by operating at discharge currents above these limits, but some fraction of the accelerator grid upstream surface will experience direct ion impingement, leading to unacceptably high sputter erosion rates.

The thrust for a given mass flow rate in the beam $\dot{m}_{ib}$ and exhaust velocity u_e is related to the beam voltage V_b by the expression

$$T = \dot{m}_{ib} u_e = \left(\frac{2M_i V_b}{e}\right)^{1/2} f_i J_d C_j \phi_g \langle Z^{-1/2} \rangle. \tag{29}$$

The maximum thrust is obtained when the source is operated at the maximum discharge current,

$$T_{max} = \frac{16\pi r_c^2 \epsilon_0 C_j \phi_g V_b^{1/2} V_t^{3/2}}{9 C_j^* l_e^2}. \tag{30}$$

The specific impulse is given by

$$\begin{aligned} I_{sp} &= \frac{f_i C_j \phi_g}{E_r g} \left(\frac{2M_i V_b}{e}\right)^{1/2} \langle Z^{-1/2} \rangle \\ &= \frac{F_i C_j \phi_g}{g} \left(\frac{2eV_b}{M_i}\right)^{1/2} \frac{\langle Z^{-1/2} \rangle}{\langle Z^{-1} \rangle} \end{aligned} \tag{31}$$

The total power is assumed to be $P = J_b V_b + J_d V_d$, although this neglects the power required for a neutralizer cathode. With this assumption, the total efficiency can be expressed as

$$\eta = \frac{\eta_u}{(\epsilon_B/V_b + 1)} \frac{\langle Z^{-1/2} \rangle^2}{\langle Z^{-1} \rangle}, \tag{32}$$

where the propellant utilization efficiency is

$$\begin{aligned} \eta_u &= \sum_Z \frac{J_Z M_i C_j \phi_g}{Z e \dot{m}_t} = \frac{M_i f_i C_j \phi_g}{e E_r} \langle Z^{-1} \rangle \\ &= F_i C_j \phi_g \end{aligned} \tag{33}$$

and the beam ion production cost is defined as

$$\epsilon_B = \frac{J_d V_d}{J_b} = \frac{V_d}{f_i C_j \phi_g} \tag{34}$$

Finally, the thrust-to-power ratio can be written as

$$T/P = \frac{(2M_i V_b/e)^{1/2} \langle Z^{-1/2} \rangle}{V_b/J_d + \epsilon_B} \qquad (35)$$

These equations demonstrate what cathode material properties, thruster design parameters and operating conditions influence VAIT performance. The VAIT thrust depends on the material properties M_i, f_i and the charge state distribution factor $\langle Z^{-1/2} \rangle$. The dependence on the charge state distribution is somewhat weaker in the VAIT compared to the VAT, which scales with $\langle Z^{-1} \rangle$. The thrust also depends on the engine design through the parameters C_j and ϕ_g. Maximizing the fraction of ion current captured by the grids drives designs toward close spacing between the cathode and the grids and a large grid radius compared to the cathode radius, as Fig. (9) shows. However, this design approach may exceed the current extraction capabilities of the ion optics. As Eq. (30) shows, the maximum thrust is obtained for the optimum combination of the geometry parameters $r_c^2 C_j \phi_g / C_j^* l^2$. There is an interesting tradeoff between the competing parameters C_j and C_j^*. The appearance of the grid transparency ϕ_g shows that performance scales with open area fraction. In conventional gas discharge ion engines, performance improves with decreasing accelerator grid open area fraction because this helps prevent the loss of neutral propellant atoms. In the VAIT, however, one is not driven to this because there are very few neutrals and those that do exist in the cathode spot plume have a high probability of condensing on the thruster surfaces they contact. The thrust also depends on the operational parameters J_d and V_b, as in conventional ion engines.

There is greater flexibility to choose the specific impulse with a VAIT compared to a VAT because the ion velocity depends on the beam voltage, not the cathode spot plasma expansion velocity, as Eq. (31) shows. The I_{sp} also depends on efficient generation of ions with low droplet production through the parameter F_i and effective use of the ion flux through the engine design parameter $C_j \phi_g$.

The total thruster efficiency scales with the propellant efficiency and charge state distribution and inversely with the ratio of beam ion production cost and beam voltage. High propellant efficiency depends on choosing cathode materials with high ion current fraction and low droplet erosion (high values of F_i) and proper accelerator design (high $C_j \phi_g$). Higher efficiency is achieved by using propellants with low average charge states. Clearly the ion production cost must be minimized by choosing materials with a low burning voltage and high ion current fraction and good thruster geometry design. Higher beam voltages can be used to compensate for high ion production costs, although this will increase the I_{sp} and decrease the thrust-to-power ratio for a given discharge current, as Eq. (35) shows.

These relationships suggest the following prescription for designing vacuum arc ion thrusters to meet certain performance specifications. The cathode material must be chosen for high ion current fraction, low droplet erosion rate, low average charge state and good ignition reliability. The beam voltage is determined by the required specific impulse. The ion optics design involves choosing an accelerator grid voltage which prevents electron backstreaming from the neutralizer and a grid spacing which is sufficient to stand off the total accelerating voltage. The grid open area fraction should be maximized, but must satisfy structural and ion beamlet focusing requirements. For operation at the maximum achievable thrust, the geometric parameter $r_c^2 C_j / C_j^*$ must be maximized. Thrust levels lower than the maximum can be obtained by varying the discharge current, and under these conditions the engine performance is optimized by maximizing the parameter C_j. The discharge current and duty cycle must be chosen to give the required average thrust level, but must not result in cathode heat inputs which cause gross melting.

Model Predictions

Material and Arc Properties

Properties for various potential cathode materials used to estimate the performance of vacuum arc thrusters and vacuum arc ion engines are summarized in Table (1). The current charge state distributions were calculated from particle charge state distributions and average charge states measured in 100 A pulsed discharges [?]. The charge state distribution was sampled at about 150 μs after arc initiation; other measurements show that the average charge state

is higher for the about the first 100 μs of a pulsed discharge [?]. The parameters $\langle Z^{-1} \rangle$ and $\langle Z^{-1/2} \rangle$ were calculated from the values of f_Z in the table. Most of the erosion data are from weight loss measurements after sequences of 250 μs pulses at 100 A [?], although some are from 80–250 A discharges of several seconds duration [?] or 170–300 A arcs of 5 seconds duration [?]. The ion mass fraction F_i was calculated from the erosion rate data assuming an ion current fraction $f_i = 0.1$. As discussed above, this is typically observed in vacuum arc experiments, but is apparently not consistent with some of the erosion rate data. The ion mass fraction for chromium, gadolinium, tantalum and tungsten exceeds unity, suggesting either that the erosion rate measurements are too low or that the ion current fraction is less than 0.1. The impact of this on calculated performance is discussed below. The discharge voltage data are from experiments with 250 μs pulsed discharges at 300 A [?]. The voltage drops through the leads and the cathode material have been subtracted, so these data represent the arc burning voltage for an anode configuration which is similar to that in VAT's or VAIT's. The ion velocity measurements were sampled from 250 μs long, 100–200 A discharges [?].

Predicted Thruster Performance

The equations developed above were used with the material properties for these cathode materials to calculate potential VAT and VAIT performance. The results for the VAT shown in Table 2 assume a discharge current of 10 A and a momentum flux integral $C_t = 0.666$. This is the maximum thrust correction factor for an exponential or cosine distribution, but might be achievable in configurations with the anode and cathode faces flush. The thrust scales linearly with the discharge current, but the other performance parameters are independent of the assumed value. The maximum specific impulse and total efficiency predicted for those species for which we have all the material properties are plotted in Fig. (10). The cathode materials that appear to have the highest performance potential in a VAT are magnesium, chromium, yttrium, tantalum and tungsten, with efficiencies ranging from 0.07 to 0.12 and specific im-

pulses of 860 to 1660 s. These materials offer the best performance because of a combination of high ion velocity and high ion fraction. Some of these predictions are artificially high because of the unrealistically high value of ion mass fraction calculated from the experimental erosion rates and an ion current fraction of 0.1. These values are not self-consistent, either because the erosion rates are too low or the ion current fractions are too high. The maximum achievable value of the ion mass fraction is unity, so the effect of increasing the erosion rate or decreasing the ion current fraction to get $F_i = 1$ was explored. As shown in Table 3, this would reduce the specific impulse by 100–200 s and the efficiency by 0.02–0.04. This performance is still competitive with other technologies such as pulsed plasma thrusters that offer very small, controlled impulse bits, and the inherent scalability of vacuum arc-based concepts may provide unique advantages.

The performance predicted for VAIT's is shown in Table 2 and in Fig. (11). For these calculations we assumed a discharge current of 10 A, a beam voltage of 1000 V, a current flux integral $C_j = 0.8$ and a grid open area fraction of 0.8. These values of C_j and ϕ_g are high, but probably achievable in a carefully designed engine. As noted above, this approach also neglects the power required for a neutralizer cathode, although this would be justified if a low power neutralizer such as a field emission array cathode were used with the ion source [?]. All of the performance parameters depend on the discharge current or beam voltage, so these results represent a point design which illustrates the impact of cathode material and the performance potential. The best materials appear to be chromium, copper, yttrium, gadolinium, tantalum and tungsten, with efficiencies of 0.42–0.64 and specific impulses at this beam voltage of 4030–7140 s. The impact of varying f_i or E_r to get a realistic upper bound on the ion mass fraction F_i is shown in Table (3). This reduces the specific impulse by 400–1500 s and the efficiency by 0.04–0.2. This suggests that the peak efficiencies for the best materials would be on the order of 0.45 for a beam voltage of 1000 V. The performance could, of course, be improved with higher beam voltages, as Fig. (12) shows. In this figure the total efficiency as

a function of specific impulse is plotted for the best cathode materials. The beam voltage ranges from 500 to 5000 V over these curves and for Cr, Gd , Ta and W the ion mass fraction F_i was assumed to be equal to one. As these curves show, the efficiency exceeds 0.5 at specific impulses of 3000 to 9000 s for the different materials. Because the ion generation occurs in a length scale on the order of 10 μm in the cathode spots, these results are largely independent of the engine size. This therefore appears to be an excellent approach for miniaturizing ion engines. The performance of conventional electron bombardment engines suffers as they are scaled to small sizes because the increased surface-to-volume ratio leads to less efficient plasma production [?].

Conclusions

The models described in this paper show how the performance of vacuum arc thrusters and vacuum arc ion engines scales with cathode material, engine geometry and operating parameters. These models were used with published values of material properties and optimistic estimates of parameters such as the ion current fraction and the current and momentum flux integrals to determine upper bounds on the performance potential of VAT's and VAIT's. The model results suggest that vacuum arc thruster configurations may be capable of operating at up to 9 percent total efficiency at a specific impulse of 900–1300 s. The advantages of this configuration are that it is very simple, requires no gas feed system, and can be operated with a very simple, low mass power processing unit [?]. The model shows that vacuum arc ion thrusters are capable of much higher performance because the ion acceleration is decoupled from the plasma production process. Efficiencies of 50–60 percent for specific impulses of 3000–9000 s should be achievable in carefully designed engines. This is a very exciting result, because this performance should be largely independent of engine scale. Very small, high performance VAIT's requiring no magnets and no gas feed systems and operating at very low average power levels (in low duty cycle pulsed operation) could be an ideal propulsion system for power- and mass-constrained microspacecraft.

Current work is focused on experimentally validating these models with direct thrust and electrical measurements and further characterizing the model input parameters. Preliminary thrust measurements for a VAT with a titanium cathode yielded a thrust-to-power ratio of 2.2 μN/W [?, ?]. Using the geometry of the thruster and the measured discharge voltage, the model described here predicts a performance of 3.5 μN/W. This is reasonably good agreement, given the uncertainties in the electrode geometry [?]. Additional thrust measurements using the thruster shown in Fig. (4) with different cathode materials, electrode geometries and discharge currents will be performed to further validate the model. Measurements of the electrical parameters and direct thrust measurements for the VAIT shown in Fig. (8) with various materials, geometries and operating conditions will be used to verify the VAIT model predictions. In addition, vacuum arc plasma sources are being characterized in a special ultra-high vacuum facility. The purpose of these experiments is to verify the model assumptions and measure the model input parameters such as erosion rates, ion current fractions, charge state distributions, angular ion current density distributions, ion velocities and discharge voltages [?].

Additional engineering challenges will have to be overcome to realize the potential of vacuum arc plasma sources. Arc ignition reliability with the triggerless method is an important issue, although preliminary tests demonstrating up to 1 million discharges are encouraging [?]. Uniform erosion of the cathode must be achieved and a reliable method of dispensing the consumable cathode must be developed. The threat of spacecraft contamination by condensible metal propellants has to be addressed. Finally, adequate engine lifetime must be demonstrated, which will require a thorough understanding of potential failure modes such as insulator and grid erosion and electrical shorts from metal vapor or macroparticle deposition. These are certainly challenging issues, but the predicted performance and scalability of vacuum arc-based thruster concepts indicate that the effort is justified. The unusual conditions achieved in vacuum arc discharges provide unique advantages for advanced propulsion systems.
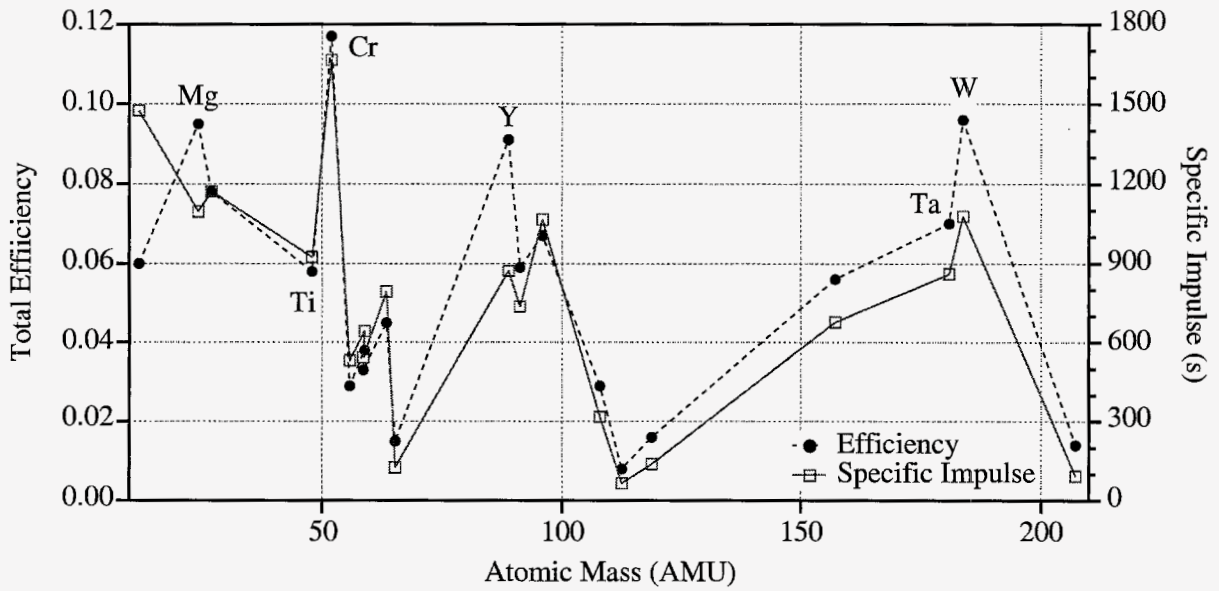
Figure 10: Predicted performance of vacuum arc thrusters for various cathode materials.
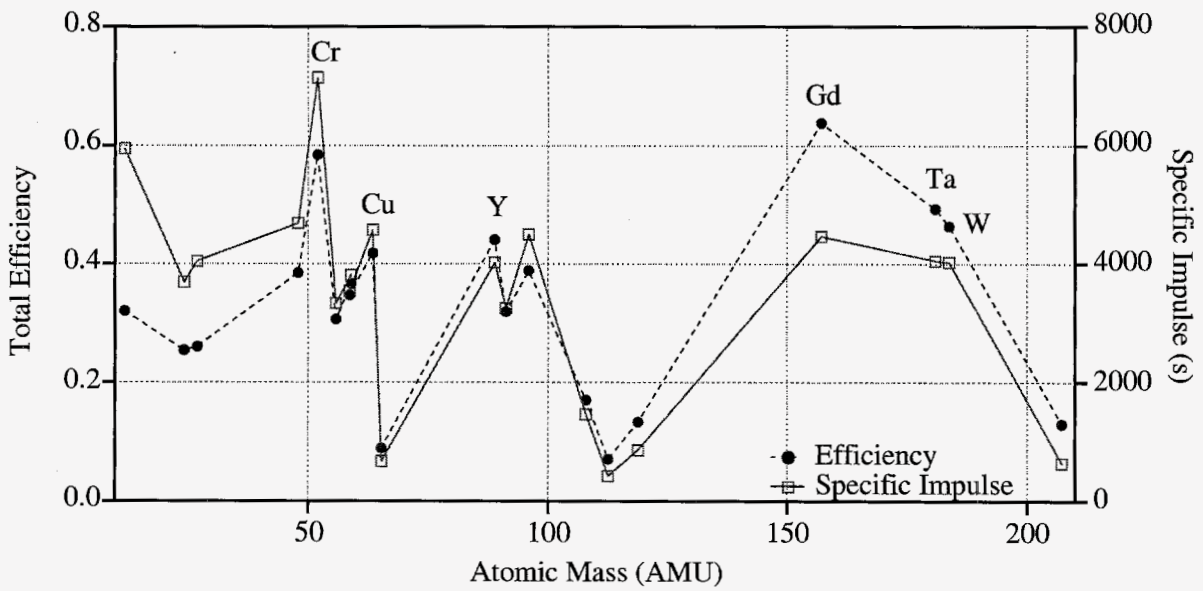

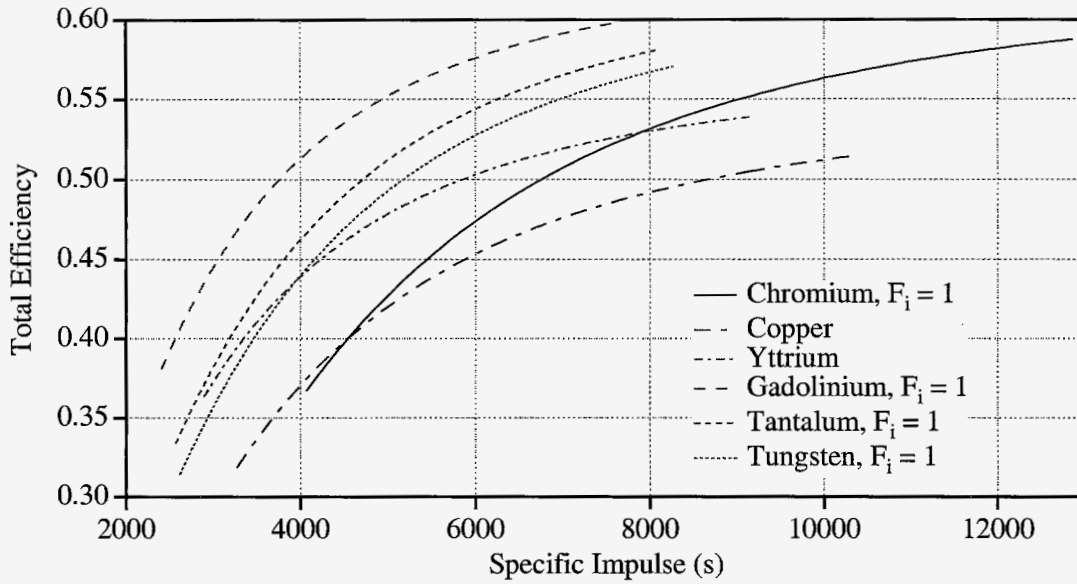Figure 11: Predicted performance of vacuum arc ion thrusters for various cathode materials.

Figure 12: Variation of VAIT efficiency with specific impulse for beam voltages ranging from 500 to 5000 V.

Species	Mass M_i (AMU)	Ion Charge State Distribution								Erosion Rate E_r (μg/C)	Ion Fraction F_i	Discharge Voltage V_d (V)	Ion Velocity u_i (m/s)
		f_1	f_2	f_3	f_4	f_5	f_6	$\langle Z^{-1}\rangle$	$\langle Z^{-1/2}\rangle$				
Li	6.941	1.000						1.00	1.00			23.5	23800
C	12	1.000						1.00	1.00	17	0.732	29.6	29700
Mg	24.305	0.307	0.701					0.66	0.80	31	0.528	18.8	30600
Al	26.981	0.224	0.590	0.191				0.58	0.75	28	0.577	23.6	29900
Si	28.086	0.450	0.504	0.043				0.72	0.83			27.5	25800
Ca	40.08	0.042	0.943	0.016				0.52	0.72			23.5	25900
Sc	44.96	0.150	0.749	0.101				0.56	0.74			19.1	
Ti	47.9	0.052	0.739	0.207				0.49	0.69	30	0.815	21.3	16700
V	50.94	0.038	0.664	0.280	0.019			0.47	0.68			22.5	19300
Cr	52	0.048	0.638	0.296	0.019			0.47	0.68	20	1.265	22.9	19400
Mn	54.94	0.327	0.658	0.020				0.66	0.80			22	10800
Fe	55.85	0.139	0.747	0.115				0.55	0.73	48	0.663	22.7	11800
Co	58.93	0.200	0.682	0.121				0.58	0.75	44	0.802	22.8	11800
Ni	58.71	0.167	0.727	0.102				0.56	0.74	47	0.736	20.5	10900
Cu	63.55	0.080	0.612	0.291	0.019			0.49	0.69	35	0.914	23.4	12800
Zn	65.38	0.667	0.333					0.83	0.90	320	0.176	15.5	10400
Ge	69.74	0.429	0.571					0.71	0.83			17.5	11000
Sr	87.62	0.010	0.990					0.50	0.71			18	
Y	88.91	0.022	0.544	0.434				0.44	0.66	45	0.898	18.1	14300
Zr	91.22	0.004	0.364	0.523	0.109			0.39	0.62	53	0.691	23.4	15700
Nb	92.91	0.003	0.160	0.510	0.293	0.033		0.33	0.57			27	15500
Mo	95.94	0.006	0.137	0.480	0.327	0.049		0.33	0.57	36	0.903	29.3	17400
Pd	106.4	0.121	0.713	0.144	0.021			0.53	0.72			21.3	15700
Ag	107.87	0.062	0.570	0.350	0.019			0.47	0.68	140	0.373	23.6	12500
Cd	112.41	0.523	0.485					0.77	0.87	620	0.142	16	6800
In	114.82	0.471	0.507					0.73	0.83			17.5	5500
Sn	118.69	0.313	0.693					0.66	0.80	295	0.273	17.5	7500
Ba	137.33	0.000	1.000					0.50	0.71			18.3	6700
La	138.91	0.005	0.685	0.311				0.45	0.67			17.2	7000
Ce	140.12	0.014	0.787	0.199				0.47	0.69			17.9	7000
Pr	140.91	0.014	0.613	0.373				0.44	0.66			20	8700
Nd	144.24		0.765	0.235				0.46	0.68			19.7	
Sm	150.4	0.010	0.779	0.211				0.47	0.68			14.6	7400
Gd	157.25	0.009	0.691	0.300				0.45	0.67	55	1.347	21.6	7400
Dy	162.5	0.009	0.574	0.417				0.43	0.66			19.8	7400
Ho	164.93	0.009	0.574	0.417				0.43	0.66			20	8300
Er	167.26	0.004	0.534	0.445	0.017			0.42	0.65			19	8200
Yb	173.04	0.014	0.867	0.118				0.49	0.70			14.4	
Hf	178.49	0.010	0.164	0.522	0.287	0.017		0.34	0.58			24.3	9200
Ta	180.95	0.007	0.225	0.389	0.328	0.051		0.34	0.58	56	1.143	28.7	11100
W	183.85	0.006	0.147	0.413	0.333	0.080	0.019	0.32	0.56	55	1.111	31.9	14300
Ir	192.22	0.019	0.278	0.519	0.165	0.019		0.38	0.61			24.5	
Pt	195.09	0.057	0.663	0.260	0.019			0.48	0.69			22.5	6800
Au	196.97	0.070	0.761	0.168				0.51	0.71			19.7	5800
Pb	207.2	0.225	0.780					0.62	0.78	510	0.257	15.5	5400
Bi	208.98	0.692	0.291					0.84	0.90			15.6	4200
Th	232.04	0.000	0.166	0.124	0.166			0.17	0.27			23.3	9900
U	231.04		0.075	0.547	0.377			0.31	0.56			23.5	11400

Table 1: Material and Arc Properties for Potential Cathode Materials

Species	Mass Flow Rate, $\dot{m}_t$ (mg/s)	Vacuum Arc Thruster				Vacuum Arc Ion Thruster					
		Thrust T (mN)	I_{sp} (s)	Total Efficiency η	Thrust-to-Power T/P (μN/W)	Thrust T (mN)	I_{sp} (s)	Propellant Efficiency η_u	Ion Production Cost ϵ_B (eV/ion)	Total Efficiency η	Thrust-to-Power T/P (μN/W)
Li		1.14			0.05	7.68			367		8.77
C	0.17	2.46	1475	0.060	0.08	10.09	5949	0.468	463	0.320	10.78
Mg	0.31	3.33	1096	0.095	17.73	11.42	3689	0.338	294	0.254	13.79
Al	0.28	3.20	1172	0.078	13.64	11.30	4044	0.370	369	0.260	12.90
Si		3.60			0.13	11.11			430		12.14
Ca		3.71			0.15	9.56			367		10.92
Sc						10.92			298		13.14
Ti	0.3	2.70	924	0.058	12.77	14.04	4689	0.522	333	0.385	16.46
V		3.17			0.13	9.72			352		11.24
Cr	0.2	3.27	1666	0.117	14.28	14.26	7143	0.810	358	0.585	16.41
Mn		2.69			0.12	14.21			344		16.52
Fe	0.48	2.50	531	0.029	11.01	15.95	3329	0.424	355	0.306	18.40
Co	0.44	2.77	643	0.038	12.17	16.75	3815	0.514	356	0.367	19.30
Ni	0.47	2.51	544	0.033	12.24	16.61	3540	0.471	320	0.347	19.65
Cu	0.35	2.73	794	0.045	11.65	15.98	4575	0.585	366	0.418	18.29
Zn	3.2	3.91	125	0.015	0.24	21.26	666	0.113	242	0.089	26.74
Ge		3.78			0.20	17.38			273		21.33
Sr						13.78			281		16.80
Y	0.45	3.85	872	0.091	21.27	18.06	4020	0.575	283	0.441	21.99
Zr	0.53	3.83	737	0.059	16.38	17.20	3251	0.443	366	0.319	19.68
Nb		3.31			0.12	9.36			422		10.29
Mo	0.36	3.77	1066	0.067	12.85	16.16	4498	0.578	458	0.389	17.32
Pd		6.13			0.28	15.99			333		18.74
Ag	1.4	4.30	317	0.029	0.18	20.45	1463	0.239	369	0.170	23.34
Cd	6.2	4.00	66	0.008	0.24	26.51	428	0.091	250	0.071	33.13
In		3.25			0.18	23.30			273		28.59
Sn	2.95	4.02	139	0.016	22.95	25.30	859	0.174	273	0.133	31.05
Ba		3.18			0.16	17.07			286		20.75
La		3.02			0.17	15.47			269		19.05
Ce		3.21			0.17	16.35			280		19.96
Pr		3.76			0.18	15.37			313		18.30
Nd						16.13			308		19.27
Sm		3.61			0.23	16.78			228		21.35
Gd	0.55	3.65	677	0.056	16.90	24.51	4466	0.862	338	0.638	28.64
Dy		3.61			0.17	16.15			309		19.27
Ho		4.11			0.20	16.27			313		19.37
Er		4.01			0.20	15.97			297		19.24
Yb						18.69			225		23.84
Hf		3.87			0.15	13.29			380		15.05
Ta	0.56	4.70	861	0.070	16.49	22.64	4050	0.732	448	0.493	24.42
W	0.55	5.80	1078	0.096	18.24	22.12	4029	0.711	498	0.464	23.06
Ir						15.19			383		17.16
Pt		4.40			0.19	19.57			352		22.62
Au		4.00			0.19	20.76			308		24.80
Pb	5.1	4.71	94	0.014	30.39	32.36	636	0.164	242	0.129	40.70
Bi		5.18			0.31	36.00			244		45.23
Th		2.62			0.11	7.35			364		8.42
U		5.72			0.23	13.93			367		15.92

Table 2: Predicted Performance of Vacuum Arc Thrusters and Vacuum Arc Ion Thrusters

Species	Erosion Rate, E_r (μg/C)	Ion Current Fraction f_i	Ion Mass Fraction F_i	Vacuum Arc Thruster			Vacuum Arc Ion Thruster			
				I_{sp} (s)	Total Effici-ency η	Thrust-to-Power T/P (μN/W)	I_{sp} (s)	Propellant Efficiency η_u	Total Effici-ency η	Thrust-to-Power T/P (μN/W)
Cr	20	0.100	1.265	1666	0.117	14.3	7143	0.81	0.585	16.4
	20	0.079	1.000	1316	0.073	11.3	5643	0.64	0.432	15.3
	25.3	0.100	1.000	1317	0.092	14.3	5647	0.64	0.462	16.4
Gd	55	0.100	1.347	677	0.056	16.9	4464	0.86	0.638	28.6
	55	0.074	1.000	501	0.031	12.5	3304	0.64	0.434	26.3
	74	0.100	1.000	503	0.042	16.9	3319	0.64	0.474	28.6
Ta	56	0.100	1.143	861	0.070	16.5	4050	0.73	0.493	24.4
	56	0.087	1.000	749	0.053	14.4	3523	0.64	0.410	23.3
	64	0.100	1.000	754	0.061	16.5	3544	0.64	0.432	24.4
W	55	0.100	1.111	1078	0.096	18.2	4029	0.71	0.464	23.1
	55	0.090	1.000	970	0.078	16.4	3626	0.64	0.402	22.2
	61	0.100	1.000	972	0.087	18.2	3632	0.64	0.418	23.1

Table 3: Effect of decreased ion mass fraction or increased erosion rate on performance.

A Theoretical Analysis of Vacuum Arc Thruster Performance *

James E. Polk, Mike Sekerak and John K. Ziemer
Jet Propulsion Laboratory, M/S 125-109, 4800 Oak Grove Drive, Pasadena, CA 91109
(818) 354-9275, james.e.polk@jpl.nasa.gov

Jochen Schein, Niansheng Qi and Robert Binder
Alameda Applied Sciences Corp, 2235 Polvorosa Ave, San Leandro, CA 94577
(510) 483-4156, schein@aasc.net

André Anders
Lawrence Berkeley National Laboratory, 1 Cyclotron Road, Berkeley, CA 94720
(510) 486-6745, aanders@lbl.gov

In vacuum arc discharges the current is conducted through vapor evaporated from the cathode surface. In these devices very dense, highly ionized plasmas can be created from any metallic or conducting solid used as the cathode. This paper describes theoretical models of performance for several thruster configurations which use vacuum arc plasma sources. This analysis suggests that thrusters using vacuum arc sources can be operated efficiently with a range of propellant options that gives great flexibility in specific impulse. In addition, the efficiency of plasma production in these devices appears to be largely independent of scale because the metal vapor is ionized within a few microns of the cathode electron emission sites, so this approach is well-suited for micropropulsion.

Introduction

Vacuum arcs, or discharges burning in metal vapor liberated from the cathode into an interelectrode gap initially at vacuum, produce high velocity, highly ionized plasma flows which can be exploited for propulsion applications. On cathode surfaces which are too cold to support bulk thermionic emission, current continuity across the metal-vacuum interface is maintained through one or more highly mobile, luminous spots. Although the bulk cathode temperature is relatively low, the local temperature in these spots is well over the boiling point of the cathode material and electrons are emitted by a combination of thermal and field emission. These emission sites are initiated at locations where there are local micro-

protrusions or dielectric inclusions which cause local enhancement of the applied electric field. Field emission in these regions causes explosive vaporization of the microprotrusion or inclusion due to very rapid Joule heating. A combination of Joule heating and ion bombardment heating sustains the temperatures required to emit electrons and vaporize cathode material. The loss of cathode material causes the formation of a tiny crater on the surface. As the crater diameter grows, the power deposition by ohmic heating and ion bombardment decreases. Eventually the temperature drops to the point where it is no longer possible to sustain electron and vapor emission and the site extinguishes. The characteristic site lifetime appears to be on the order of a few tens of nanoseconds [?]. The resulting craters have a diameter that is typically only 1-10 microns [?], although gross melting may result in larger structures [?]. The extinction of an emission site is generally followed by the igni-

tion of a new site at a nearby microprotrusion, often apparently self-generated by the molten metal flows from the previous site. The luminous spot therefore appears to move over the cathode surface.

Extraordinary conditions are achieved in the cathode spots. Current densities on the order of 10^8 A/cm^2 [?] in the emission site and heat fluxes of 10^8–10^9 W/cm^2 [?] produce rapid vaporization and ionization of the cathode material. Plasma densities in the near-cathode region reach 10^{20}–10^{21} cm^{-3} [?], nearly the density of the solid metal. The plasma is generally almost 100 percent ionized, often with multiple charge states [?]. What is truly remarkable is how easy it is to generate these conditions in cold cathode arc discharges. These extreme environments lead to vigorous acceleration of the metal vapor plasma away from the cathode spot, and velocities achieved in the expanding plasma plume are typically on the order of 10^4 m/s [?].

Vacuum arc-generated plasmas can be used in several different types of propulsion devices. The plasma plumes produced in cathode spots are highly directional, and can be used to produce thrust directly. Vacuum arcs may also be used as plasma sources in ion accelerators such as ion or Hall thrusters. The focus of this paper is on application of vacuum arc discharges in thermal Vacuum Arc Thrusters (VAT's) and in electrostatic Vacuum Arc Ion Thrusters (VAIT's). The unique physical conditions achieved in vacuum arcs offer several potential advantages in these devices. A highly ionized plasma is generated very efficiently in cathode spot operation. Because the ionization process occurs within tens of microns of the emission site, the plasma source is inherently scalable to very small sizes for micropropulsion applications. No magnetic field is required for an efficient discharge, as in electron bombardment ion engines. Vacuum arc discharges can be operated in pulses with no sacrifice in plasma production efficiency, so the duty cycle can be varied to match the engine power to that available from the spacecraft. This can enable the use of high specific impulse electric thrusters for power-constrained microspacecraft. Finally, because the propellant is provided by the consumable cathode, no gas feed system is necessary. This not only reduces mass and volume, but

eliminates the need for low leak-rate valves. It is very difficult to achieve low leak rates in microfabricated valves, so this is a significant advantage over conventional ion engines for microspacecraft applications.

Vacuum arc discharges exhibit certain regularities in their behavior which allow simple, semi-empirical models of thruster performance. The purpose of the models developed in this paper is to provide guidance in choosing cathode materials and explore the performance potential of several implementations of vacuum arc thrusters. We will first describe the performance models and then discuss the performance characteristics of a number of candidate propellants.

A Semi-Empirical Performance Model

Vacuum Arc Plasma Sources

Mass is eroded from cathode spots in the form of metal vapor ions, droplets or "macroparticles," and neutral vapor [?], although the majority of the neutral vapor appears to be evaporated from the macroparticles in flight [?]. For sufficiently low values of energy deposited in the cathode (low average current density and/or short pulses), the total erosion rate $\dot{m}_t$ scales with the arc discharge current J_d [?],

$$\dot{m}_t = E_r J_d, \qquad (1)$$

The erosion rate E_r is constant in this regime because the mass loss occurs primarily within single, isolated emission sites. Higher current levels are accommodated by more emission sites. Above a certain threshold current or during long pulses the temperature fields of individual emission sites may overlap and cause gross melting. Under these conditions the droplet erosion rate may increase dramatically [?].

The ion component of the mass flux can be described as an ion current J_i, which is the sum of the currents J_Z associated with the fluxes of ions in various charge states Z. Experiments over a wide range of conditions show that the ion current in the spot plasma plume can be expressed as a nearly constant fraction f_i of the discharge current ranging from 0.07 to 0.1 [?]. We can therefore write the ion flow in the cathode spot plasma as

$$J_i = \sum_Z J_Z = f_i J_d \qquad (2)$$

and the ion mass flow rate as

$$\dot{m}_i = \sum_Z \frac{J_Z M_i}{Ze} = \frac{f_i J_d M_i}{e} \langle Z^{-1} \rangle, \quad (3)$$

where e is the charge on an electron, M_i is the mass of the ion, $\langle Z^{-1} \rangle$ represents the mean inverse charge state,

$$\langle Z^{-1} \rangle = \sum_Z \frac{f_Z}{Z}. \quad (4)$$

and f_Z is the ratio of the current due to a single charge state to the total ion current,

$$f_Z = \frac{J_Z}{J_i}. \quad (5)$$

This charge state distribution is assumed to be constant for a given cathode material. An equilibrium composition of multiply charged ions is created in the hot, high density metal vapor plasma near the emission zone and "freezes" at some point in the plume from the cathode spot as the recombination rate drops due to plasma expansion and cooling. Measurements in pulsed discharges show that the charge state distribution for a certain material changes over the first 100 μs of the discharge and then becomes relatively constant [?]. The charge state distribution does not vary significantly with discharge current over a range of 50-400 A [?], but may be influenced by applied magnetic fields [?] and higher discharge currents [?]. The fraction of the total mass loss that occurs in the form of ions is given by the expression

$$F_i = \frac{f_i M_i \langle Z^{-1} \rangle}{e E_r}. \quad (6)$$

The plasma is accelerated to high velocities within a few hundred microns of the cathode spot by gas-dynamic (electron pressure gradient and electron-ion friction) forces and possibly by electrostatic forces created by a potential hump that forms above the emission site [?]. Experimental measurements of the ion current density in the plume expanding from the cathode region in vacuum arcs suggest that it follows a cosine [?] or exponential distribution [?]. The geometry used in defining these distributions is shown in Fig. (1). For a cosine distribution in polar coordinates the current density at a radius l and angle ϕ
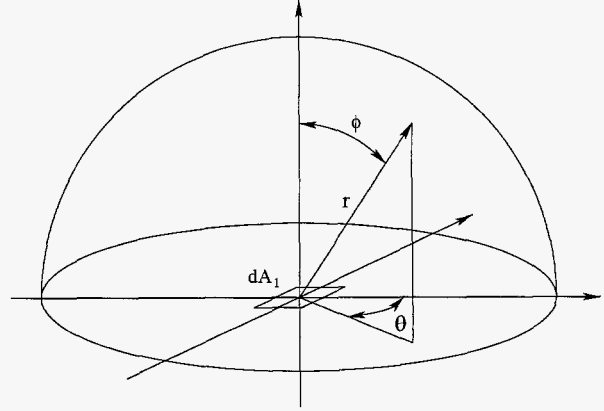

Figure 1: Geometry used to define ion current distribution.
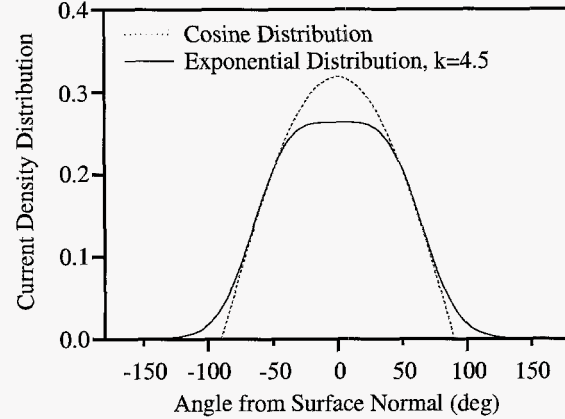

Figure 2: Normalized angular ion current distribution for cosine and exponential functions.

defined from the surface normal due to mass generated in area dA_1 on the cathode surface is

$$j_{ip}(l, \phi) = \frac{j_{ic} \cos \phi \, dA_1}{\pi l^2} \quad (7)$$

where j_{ic} is the ion current flux from the cathode surface. This function normalized to a value of $j_{ic} dA_1 = 1$ is plotted in Fig. (2).

The cosine distribution is naturally truncated at $\phi = 90$ degrees, but ion current is often observed at higher angles [?]. This ion backflow is obviously not generated at the cathode surface but is the result of forces acting on the plasma plume away from the electrode structure. The exponential distribution assumes that the current drops exponentially with the solid angle subtended by the polar angle ϕ. This distribution often more accurately captures the ion cur-

rent density at high angles, and as shown in Fig. (2), permits ion current backflow. This distribution is given by

$$j_{ip}(l, \phi) = \frac{2j_{ic}dA_1}{\sqrt{\pi}l^2 k \, \mathrm{erf}(2\pi/k)} \times \exp(-[2\pi(1 - \cos\phi)]^2/k^2), \quad (8)$$

where k is a constant which determines the spread in the distribution. With the assumptions discussed above, the ion current density at the cathode surface can be written as $j_{ic} = f_i j_d$. The ion mass flow rate at the point (l, ϕ) due to erosion at dA_1 is given by

$$\dot{m}_{ip}(l, \phi) = \frac{M_i j_{ip}}{e}\langle Z^{-1} \rangle. \quad (9)$$

This relationship relies on the assumption that the charge state distribution is independent of angle, so that $j_Z/j_{ip} = f_Z$ everywhere in the plume. Some angular variation in charge state distribution due to electric fields in the plume and charge exchange with neutral atoms evaporated from macroparticles at high angles is calculated theoretically [?] or observed in experiments [?]. These effects are not expected to significantly affect the calculated performance, however.

The ion velocity u_i is assumed to be a constant for all ion charge states of a given material. This is justified by experimental data which generally show that the velocity does not vary significantly with current or angle [?]. A weak variation with charge state is observed, apparently due to XXX [?]. The discharge voltage V_d is also assumed to be constant for a given cathode material. This is also justified by experiment, which shows that the burning voltage for a given material is dominated by the cathode fall [?]. The voltage does vary weakly with anode geometry [?] and significant voltage drops can occur in current leads or the cathode material itself [?].

Vacuum Arc Thruster Performance

In the vacuum arc thruster (VAT) the expanding cathode spot plasma is used to produce thrust. The general configuration of a thruster developed by Alameda Applied Sciences Corporation [?] is shown in Fig. (3). Figure (4) shows a photograph of a VAT with a titanium cathode and molybdenum anode that was built and tested at JPL. This design consists of a
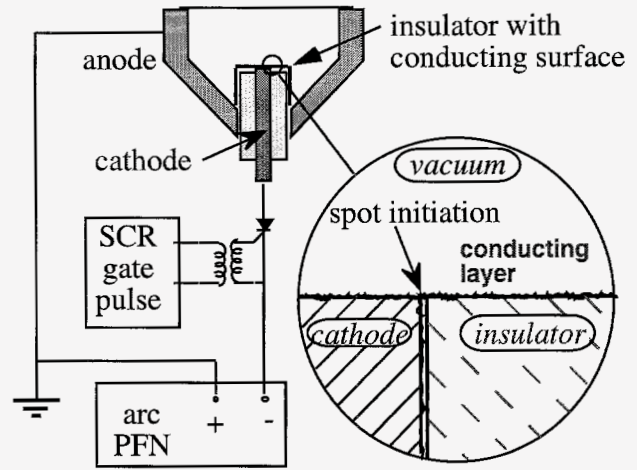

Figure 3: Schematic of a vacuum arc thruster.

Figure 4: Photograph of a laboratory model vacuum arc thruster.

central rod-shaped cathode separated from a coaxial anode by a thin-walled insulating tube. The face of the cathode and insulator may in general be recessed from the anode face. The consumable cathode rod would have to be fed into the discharge region as material is eroded from it. Inductively or capacitively driven pulsed discharges are ignited in this configuration by what is called "triggerless" operation [?]. A thin conducting film on the surface of the insulator produces a high but finite impedance between the cathode and anode. When a relatively low voltage of several hundred volts is applied between the electrodes breakdown occurs at very small gaps or flaws in the thin metal film. These tiny discharges produce enough metal vapor to initiate the main discharge in the gap. Metal vapor and droplets eroded from the cathode replenish the thin conducting layer on the insulator.

The thrust for this configuration can be derived by integrating the momentum flux through the aperture in the anode plane. The geometry used to calculate the thrust is shown in Fig. (5). The differential thrust due to ion flux from area dA_1 on the cathode surface through area dA_2 at the anode exit plane is
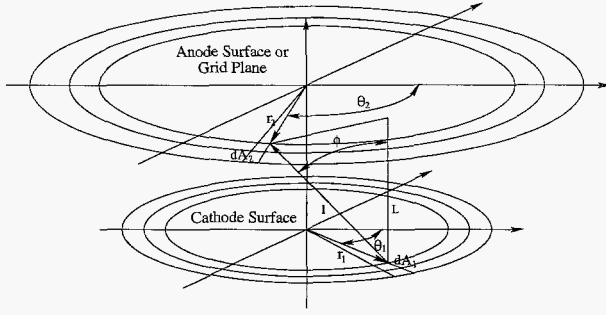
Figure 5: Geometry used to calculate the momentum flux through the anode plane.

given by

$$
\begin{aligned}
dT &= d\dot{m}_{ip}(l,\phi)(u_i\cos\phi)(\cos\phi dA_2) \\
&= \frac{M_i j_{ip}}{e}\langle Z^{-1}\rangle u_i \cos^2\phi dA_2.
\end{aligned} \tag{10}
$$

Integrating this over the cathode surface and the anode exit plane yields the expression

$$
T = \frac{M_i f_i J_d u_i}{e}\langle Z^{-1}\rangle C_t(\overline{L},\overline{r}_a), \tag{11}
$$

which represents the thrust that would be achieved if all of the eroded ion flux exited the engine with a velocity u_i directed along the axis multiplied by a thrust correction factor C_t which accounts for plume divergence and deposition of eroded cathode material on the anode interior walls. This expression also assumes that the discharge current density is uniform over the cathode surface, $j_d = J_d/\pi r_c^2$, where r_c is the cathode radius. In any single discharge this assumption is violated because the current is highly nonuniform, concentrated in individual cathode spots. This approach will give the correct average thrust over many discharges if the erosion rate of the cathode is uniform, as it must be in a good thruster design.

The thrust correction factor for a cosine distribution is given by integrating over the cathode source plane to determine the total momentum flux through a point on the anode exit plane and then integrating that result over the anode exit area. This yields

$$
C_t = \frac{\overline{L}^3}{\pi^2}\int_0^{2\pi}\int_0^{2\pi}\int_0^{\overline{r}_a}\int_0^1 \frac{\overline{r}_1\overline{r}_2 d\overline{r}_1 d\overline{r}_2 d\theta_1 d\theta_2}{\overline{l}^5}, \tag{12}
$$

where $\overline{l} = [\overline{L}^2 + \overline{r}_1^2 + \overline{r}_2^2 - 2\overline{r}_1\overline{r}_2\cos(\theta_1-\theta_2)]^{1/2}$. The thruster geometry parameters are nondimensionalized by the cathode radius, so $\overline{L} = L/r_c$ where L is the cathode length, $\overline{r}_1 = r_1/r_c$ and $\overline{r}_2 = r_2/r_c$, where r_1 and r_2 are the radii in the cathode and anode planes and $\overline{r}_a = r_a/r_c$, where r_a is the anode exit radius. The angles in the cathode and anode planes are given by θ_1 and θ_2. The corresponding thrust correction factor for the exponential distribution is

$$
C_t = \frac{2\overline{L}^2}{\pi^{3/2}k\,\mathrm{erf}(2\pi/k)}I_1 \tag{13}
$$

where

$$
I_1 = \int_0^{2\pi}\int_0^{2\pi}\int_0^{\overline{r}_a}\int_0^1 \frac{\exp(\frac{-[2\pi(1-\overline{L}/\overline{l})]^2}{k^2})dA_1 dA_2}{\overline{l}^4} \tag{14}
$$

and $dA_1 dA_2 = \overline{r}_1\overline{r}_2 d\overline{r}_1 d\overline{r}_2 d\theta_1 d\theta_2$. These integrals were evaluated numerically for a range of electrode geometry parameters $\overline{L}$ and $\overline{r}_a$ and plotted in Fig. (6). For the exponential distribution a spread factor $k = 4.5$ was chosen, based on measurements made with a copper vacuum arc discharge at 100 A [?]. The maximum thrust is achieved when the anode and cathode surfaces are coplanar, so the anode does not shadow the plasma flux. With this geometry, the thrust coefficient is 0.67 for a cosine distribution and 0.64 for an exponential distribution with $k = 4.5$. This maximum thrust coefficient represents the thrust loss due to plume divergence alone.

The specific impulse for a VAT is given by the expression

$$
\begin{aligned}
I_{sp} &= \frac{T}{\dot{m}_t g} = \frac{M_i f_i u_i C_t}{eE_r g}\langle Z^{-1}\rangle \\
&= \frac{F_i u_i C_t}{g}.
\end{aligned} \tag{15}
$$

The power consumed in this simple device is just the discharge power, $P = J_d V_d$. The total efficiency can therefore be expressed as

$$
\eta = \frac{T^2}{2\dot{m}_t P} = \frac{M_i^2 f_i^2 u_i^2 C_t^2(\langle Z^{-1}\rangle)^2}{2e^2 E_r V_d}, \tag{16}
$$

and the thrust-to-power ratio is

$$
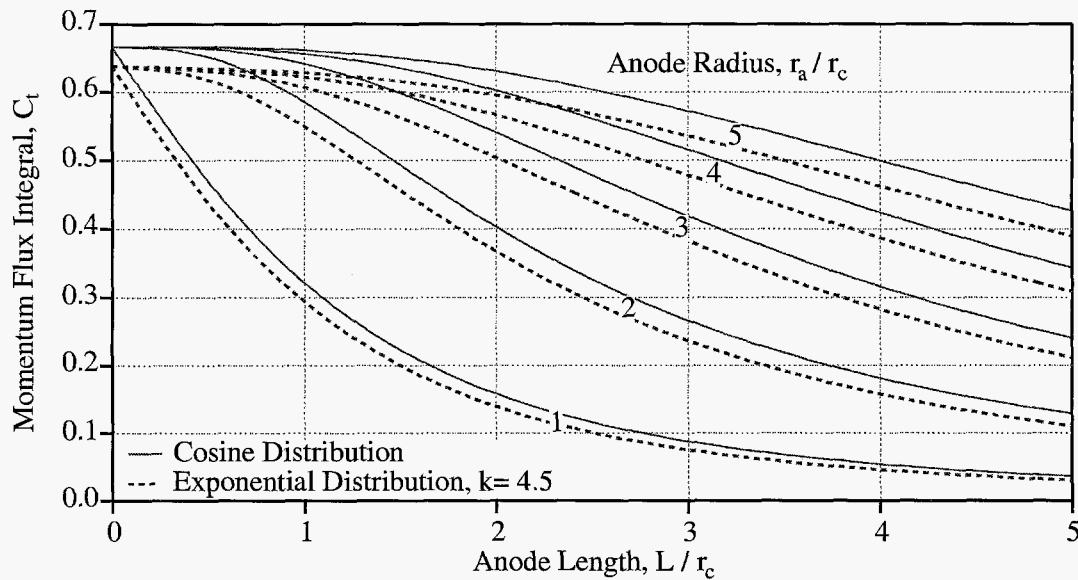T/P = \frac{M_i f_i u_i C_t}{eV_d}\langle Z^{-1}\rangle. \tag{17}
$$

Figure 6: Thrust factor which corrects for plume divergence and loss of plasma to anode walls.

The thrust of a VAT scales with the ion mass M_i, ion current fraction f_i, plasma velocity u_i and the charge state distribution factor $\langle Z^{-1} \rangle$, which are fundamentally cathode material properties. It also scales with the discharge current J_d, which is limited to values greater than the chopping current (the minimum value required to sustain a vacuum arc discharge) and less than the threshold for gross melting. The thrust also depends on the thrust coefficient C_t, which argues for an electrode geometry in which the anode does not intercept the cathode spot plasma, such as flush anode and cathode faces. However, other considerations may affect this conclusion. The discharge voltage will depend to some extent on electrode geometry and will likely be higher if the anode surface is not in good contact with the low impedence plasma. Because the droplet flux from the cathode is peaked at high angles (i.e. along the cathode surface) [?], most of the droplets will be captured on the interior anode wall in geometries with a recessed cathode. Some loss in thrust and efficiency may be tolerable if it results in less mass deposition on the spacecraft.

The specific impulse also depends on the material properties and the geometry, but varies inversely with the cathode erosion rate E_r. For a fixed ion current fraction f_i, a lower total erosion rate implies lower droplet erosion, a mass flux from the consumable cathode which does not contribute significantly to the thrust. The I_{sp} is independent of the discharge current because the plasma acceleration occurs in individual cathode spots for low currents. Increasing the discharge current changes the number of active emission sites, but does not influence the fundamental acceleration mechanism. At higher current levels interactions between spots may lead to additional electromagnetic or electrothermal acceleration, but this will likely occur under conditions which also lead to gross melting and intolerable droplet erosion. The total efficiency scales with the squares of the thrust parameters, inversely with erosion rate and discharge voltage and is independent of discharge current. This underscores the importance of designs which minimize voltage drops in the current leads, cathode structure and interelectrode plasma. For many power-limited micropropulsion applications the thrust-to-power ratio is a critical parameter. To maximize the T/P, cathode material with high values of the parameters M_i, f_i, u_i and low charge state distributions should be chosen and the electrode geometry should be designed to maximize the parameter C_t/V_d.

Vacuum Arc Ion Thruster Performance

In Vacuum Arc Ion Thrusters (VAIT's) a device like the VAT is used to supply a plasma which is

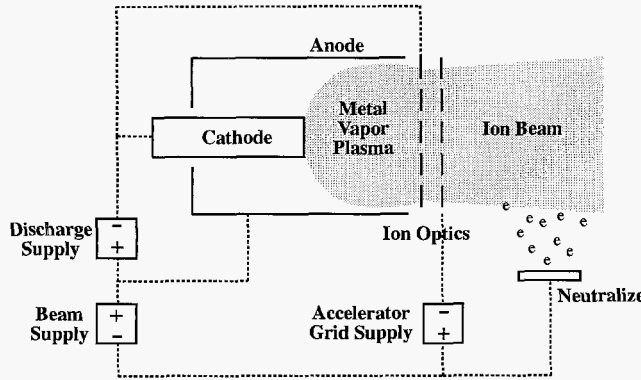Figure 8: Photograph of a laboratory model vacuum arc ion thruster.

Figure 7: Schematic of a vacuum arc ion thruster.

then accelerated electrostatically with ion optics. A schematic of this implementation with two grid ion optics is shown in Fig. (7), and Fig. (8) shows a photograph of a laboratory model thruster built by JPL and Alameda Applied Sciences Corporation. VAIT's are more complex than the VAT discussed above, but offer much higher performance potential because the ion acceleration process is decoupled from the plasma production.

The operation of the plasma source for the VAIT is assumed to be like that described by the model discussed above. The beam current is given by the fraction of the total arc ion current which is extracted by the ion optics,

$$J_b = f_i J_d C_j \phi_g. \tag{18}$$

The fraction of the total ion current $f_i J_d$ intercepted by the grids is given by the parameter C_j and the fraction of that accelerated through the ion optics is given by the grid transparency ϕ_g. The current fraction incident on the grids is determined by integrating the current flux from the cathode over the grid area, similar to the procedure used above to determine the momentum flux integral. For a cosine distribution this yields

$$C_j = \frac{\overline{L}^2}{\pi^2} \int_0^{2\pi}\int_0^{2\pi}\int_0^{\overline{r}_g}\int_0^1 \frac{\overline{r}_1 \overline{r}_2 d\overline{r}_1 d\overline{r}_2 d\theta_1 d\theta_2}{\overline{l}^4}. \tag{19}$$

For an exponential distribution the optics current is

$$C_j = \frac{2\overline{L}}{\pi^{3/2} k \operatorname{erf}(2\pi/k)} I_2 \tag{20}$$

where

$$I_2 = \int_0^{2\pi}\int_0^{2\pi}\int_0^{\overline{r}_g}\int_0^1 \frac{\exp(\frac{-[2\pi(1-\overline{L}/\overline{l})]^2}{k^2}) dA_1 dA_2}{\overline{l}^3}. \tag{21}$$

and, as above, $dA_1 dA_2 = \overline{r}_1 \overline{r}_2 d\overline{r}_1 d\overline{r}_2 d\theta_1 d\theta_2$. In these expressions, L is the distance between the cathode and the screen grid, $\overline{L} = L/r_c$, r_g is the radius of the ion optics active beam area and $\overline{r}_g =$
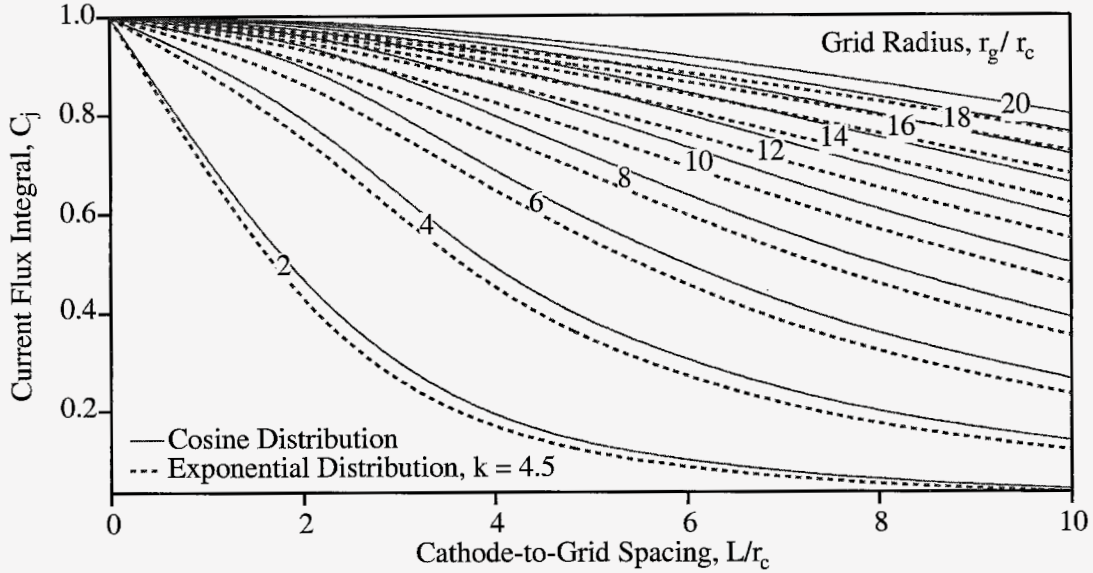
Figure 9: Geometry factor which accounts for ion current to surfaces other than the ion optics.

r_g/r_c. These integrals are plotted in Fig. (9) for a range of cathode-grid geometry parameters. As with the VAT, these relationships are not valid for a single discharge with a nonuniform distribution of current on the cathode surface, but yield the correct values averaged over many discharges if the cathode erodes uniformly. The grid transparency ϕ_g is assumed to be equal to the physical open area fraction of the screen grid. Ion optics with a quiescent upstream plasma typically exhibit an effective transparency greater than the open area fraction because the convex sheath upstream of the screen grid extracts ions from an area larger than the aperture area. In vacuum arc sources the plasma typically approaches the grid with a velocity greater than the Bohm velocity, so the ion trajectories will be less affected by the convex equipotential lines near the entrance to the screen grid aperture and the effective transparency will be close to the physical open area fraction.

Equation (18) assumes that the beam current extraction is not limited by optics focusing effects. If we model the ion optics as a plane diode, the maximum ion current density that can be extracted from the upstream plasma is given by the Child-Langmuir law [?],

$$j_b^{max} = \frac{4\epsilon_0}{9\langle Z^{-1/2}\rangle}\left(\frac{2e}{M_i}\right)^{1/2}\frac{V_t^{3/2}}{l_e^2}. \qquad (22)$$

In this expresssion, ϵ_0 is the permittivity of free space, l_e is the effective gap over which the ions are accelerated, $\langle Z^{-1/2}\rangle = \sum_Z f_Z/Z^{1/2}$, and the total accelerating voltage between the grids V_t is the difference between the beam voltage V_b and the accelerator grid voltage V_a. In reality, the current flow between the grids is always at the space charge limit; the plasma boundary (upstream sheath edge) moves, varying the effective acceleration length l_e, so that the beam current density given in Eq. (22) is consistent with the flux of ions toward the screen grid aperture. As the upstream plasma flux increases, the plasma boundary moves into the screen grid aperture, and at a certain value of the upstream density the sheath no longer properly focuses the ions through the accelerator grid aperture. This perveance limit for circular apertures is given approximately by Eq. (22) if $l_e = [l_g^2 + d_s^2/4]^{1/2}$, where l_g is the gap between the grids and d_s is the screen grid hole diameter [?]. For a VAIT, the peak ion current density at the screen grid must not exceed the value given by Eq. (22) to avoid direct ion impingement on the accelerator grid. This places a limit on the maximum discharge current (which controls the total plasma production rate and therefore the ion current density) that can be used for a given geometry.

The peak ion current density at the screen grid

depends on the distribution of discharge current on the cathode surface and the angular distribution of plasma flowing from the cathode spots. We will consider two limiting cases for each of the angular distributions considered above. The worst case condition occurs when the discharge current is below the spot-splitting current and a single cathode spot carries the entire discharge current. The peak ion current density then occurs directly above this spot. The other limiting case occurs when the discharge current is much higher than the spot splitting current and many spots are simultaneously active. In this limit the discharge current density is approximated as a uniform distribution over the entire cathode surface. The peak ion current density at the screen grid will then occur along the centerline of the thruster. In all cases the peak ion current density at the screen grid is given by an expression of the form,

$$j_{ip}^{max} = \frac{f_i J_d C_j^*(\overline{L})}{\pi r_c^2} \qquad (23)$$

where C_j^* is a geometry factor which depends on $\overline{L}$, the ratio of the distance between the cathode and the grids and the cathode radius.

For a cosine ion current density distribution the geometry parameter for operation with a single spot (low discharge currents) is

$$C_j^* = \frac{1}{\overline{L}^2}. \qquad (24)$$

For operation with many cathode spots (high discharge currents), the peak ion current density at the grids scales with the factor

$$C_j^* = \frac{1}{\overline{L}^2 + 1}. \qquad (25)$$

For an exponential distribution, single spot operation yields a peak ion current density geometry parameter of

$$C_j^* = \frac{2\sqrt{\pi}}{\overline{L}^2 k \, \text{erf}(2\pi/k)}. \qquad (26)$$

For multiple spot operation, the peak ion current density scales with

$$C_j^* = \frac{4\sqrt{\pi} \, \overline{L}}{k \, \text{erf}(2\pi/k)} \times \int_0^1 \frac{\exp(\frac{-[2\pi(1-\overline{L}/\overline{l})]^2}{k^2})\overline{r}_1 d\overline{r}_1}{l^{3/2}}. \qquad (27)$$

Equating these expressions to the space charge-limited current density defined by Eq. (22) and solving for J_d gives expressions for the maximum discharge current,

$$J_d^{max} = \frac{4\pi r_c^2 \epsilon_0}{9 f_i C_j^* \langle Z^{-1/2} \rangle} \left(\frac{2e}{M_i}\right)^{1/2} \frac{V_t^{3/2}}{l_e^2}. \qquad (28)$$

It may be possible to extract more beam current by operating at discharge currents above these limits, but some fraction of the accelerator grid upstream surface will experience direct ion impingement, leading to unacceptably high sputter erosion rates.

The thrust for a given mass flow rate in the beam $\dot{m}_{ib}$ and exhaust velocity u_e is related to the beam voltage V_b by the expression

$$T = \dot{m}_{ib} u_e = \left(\frac{2M_i V_b}{e}\right)^{1/2} f_i J_d C_j \phi_g \langle Z^{-1/2} \rangle. \qquad (29)$$

The maximum thrust is obtained when the source is operated at the maximum discharge current,

$$T_{max} = \frac{16\pi r_c^2 \epsilon_0 C_j \phi_g V_b^{1/2} V_t^{3/2}}{9 C_j^* l_e^2}. \qquad (30)$$

The specific impulse is given by

$$\begin{aligned} I_{sp} &= \frac{f_i C_j \phi_g}{E_r g} \left(\frac{2M_i V_b}{e}\right)^{1/2} \langle Z^{-1/2} \rangle \\ &= \frac{F_i C_j \phi_g}{g} \left(\frac{2eV_b}{M_i}\right)^{1/2} \frac{\langle Z^{-1/2} \rangle}{\langle Z^{-1} \rangle} \end{aligned} \qquad (31)$$

The total power is assumed to be $P = J_b V_b + J_d V_d$, although this neglects the power required for a neutralizer cathode. With this assumption, the total efficiency can be expressed as

$$\eta = \frac{\eta_u}{(\epsilon_B/V_b + 1)} \frac{\langle Z^{-1/2} \rangle^2}{\langle Z^{-1} \rangle}, \qquad (32)$$

where the propellant utilization efficiency is

$$\begin{aligned} \eta_u &= \sum_Z \frac{J_Z M_i C_j \phi_g}{Z e \dot{m}_t} = \frac{M_i f_i C_j \phi_g}{e E_r} \langle Z^{-1} \rangle \\ &= F_i C_j \phi_g \end{aligned} \qquad (33)$$

and the beam ion production cost is defined as

$$\epsilon_B = \frac{J_d V_d}{J_b} = \frac{V_d}{f_i C_j \phi_g} \qquad (34)$$

Finally, the thrust-to-power ratio can be written as

$$T/P = \frac{(2M_i V_b/e)^{1/2}\langle Z^{-1/2}\rangle}{V_b/J_d + \epsilon_B} \quad (35)$$

These equations demonstrate what cathode material properties, thruster design parameters and operating conditions influence VAIT performance. The VAIT thrust depends on the material properties M_i, f_i and the charge state distribution factor $\langle Z^{-1/2}\rangle$. The dependence on the charge state distribution is somewhat weaker in the VAIT compared to the VAT, which scales with $\langle Z^{-1}\rangle$. The thrust also depends on the engine design through the parameters C_j and ϕ_g. Maximizing the fraction of ion current captured by the grids drives designs toward close spacing between the cathode and the grids and a large grid radius compared to the cathode radius, as Fig. (9) shows. However, this design approach may exceed the current extraction capabilities of the ion optics. As Eq. (30) shows, the maximum thrust is obtained for the optimum combination of the geometry parameters $r_c^2 C_j \phi_g / C_j^* l^2$. There is an interesting tradeoff between the competing parameters C_j and C_j^*. The appearance of the grid transparency ϕ_g shows that performance scales with open area fraction. In conventional gas discharge ion engines, performance improves with decreasing accelerator grid open area fraction because this helps prevent the loss of neutral propellant atoms. In the VAIT, however, one is not driven to this because there are very few neutrals and those that do exist in the cathode spot plume have a high probability of condensing on the thruster surfaces they contact. The thrust also depends on the operational parameters J_d and V_b, as in conventional ion engines.

There is greater flexibility to choose the specific impulse with a VAIT compared to a VAT because the ion velocity depends on the beam voltage, not the cathode spot plasma expansion velocity, as Eq. (31) shows. The I_{sp} also depends on efficient generation of ions with low droplet production through the parameter F_i and effective use of the ion flux through the engine design parameter $C_j \phi_g$.

The total thruster efficiency scales with the propellant efficiency and charge state distribution and inversely with the ratio of beam ion production cost and beam voltage. High propellant efficiency depends on choosing cathode materials with high ion current fraction and low droplet erosion (high values of F_i) and proper accelerator design (high $C_j \phi_g$). Higher efficiency is achieved by using propellants with low average charge states. Clearly the ion production cost must be minimized by choosing materials with a low burning voltage and high ion current fraction and good thruster geometry design. Higher beam voltages can be used to compensate for high ion production costs, although this will increase the I_{sp} and decrease the thrust-to-power ratio for a given discharge current, as Eq. (35) shows.

These relationships suggest the following prescription for designing vacuum arc ion thrusters to meet certain performance specifications. The cathode material must be chosen for high ion current fraction, low droplet erosion rate, low average charge state and good ignition reliability. The beam voltage is determined by the required specific impulse. The ion optics design involves choosing an accelerator grid voltage which prevents electron backstreaming from the neutralizer and a grid spacing which is sufficient to stand off the total accelerating voltage. The grid open area fraction should be maximized, but must satisfy structural and ion beamlet focusing requirements. For operation at the maximum achievable thrust, the geometric parameter $r_c^2 C_j / C_j^*$ must be maximized. Thrust levels lower than the maximum can be obtained by varying the discharge current, and under these conditions the engine performance is optimized by maximizing the parameter C_j. The discharge current and duty cycle must be chosen to give the required average thrust level, but must not result in cathode heat inputs which cause gross melting.

Model Predictions

Material and Arc Properties

Properties for various potential cathode materials used to estimate the performance of vacuum arc thrusters and vacuum arc ion engines are summarized in Table (1). The current charge state distributions were calculated from particle charge state distributions and average charge states measured in 100 A pulsed discharges [?]. The charge state distribution was sampled at about 150 μs after arc initiation; other measurements show that the average charge state

is higher for the about the first 100 μs of a pulsed discharge [?]. The parameters $\langle Z^{-1} \rangle$ and $\langle Z^{-1/2} \rangle$ were calculated from the values of f_Z in the table. Most of the erosion data are from weight loss measurements after sequences of 250 μs pulses at 100 A [?], although some are from 80–250 A discharges of several seconds duration [?] or 170–300 A arcs of 5 seconds duration [?]. The ion mass fraction F_i was calculated from the erosion rate data assuming an ion current fraction $f_i = 0.1$. As discussed above, this is typically observed in vacuum arc experiments, but is apparently not consistent with some of the erosion rate data. The ion mass fraction for chromium, gadolinium, tantalum and tungsten exceeds unity, suggesting either that the erosion rate measurements are too low or that the ion current fraction is less than 0.1. The impact of this on calculated performance is discussed below. The discharge voltage data are from experiments with 250 μs pulsed discharges at 300 A [?]. The voltage drops through the leads and the cathode material have been subtracted, so these data represent the arc burning voltage for an anode configuration which is similar to that in VAT's or VAIT's. The ion velocity measurements were sampled from 250 μs long, 100–200 A discharges [?].

Predicted Thruster Performance

The equations developed above were used with the material properties for these cathode materials to calculate potential VAT and VAIT performance. The results for the VAT shown in Table 2 assume a discharge current of 10 A and a momentum flux integral $C_t = 0.666$. This is the maximum thrust correction factor for an exponential or cosine distribution, but might be achievable in configurations with the anode and cathode faces flush. The thrust scales linearly with the discharge current, but the other performance parameters are independent of the assumed value. The maximum specific impulse and total efficiency predicted for those species for which we have all the material properties are plotted in Fig. (10). The cathode materials that appear to have the highest performance potential in a VAT are magnesium, chromium, yttrium, tantalum and tungsten, with efficiencies ranging from 0.07 to 0.12 and specific im-

pulses of 860 to 1660 s. These materials offer the best performance because of a combination of high ion velocity and high ion fraction. Some of these predictions are artificially high because of the unrealistically high value of ion mass fraction calculated from the experimental erosion rates and an ion current fraction of 0.1. These values are not self-consistent, either because the erosion rates are too low or the ion current fractions are too high. The maximum achievable value of the ion mass fraction is unity, so the effect of increasing the erosion rate or decreasing the ion current fraction to get $F_i = 1$ was explored. As shown in Table 3, this would reduce the specific impulse by 100–200 s and the efficiency by 0.02–0.04. This performance is still competitive with other technologies such as pulsed plasma thrusters that offer very small, controlled impulse bits, and the inherent scalability of vacuum arc-based concepts may provide unique advantages.

The performance predicted for VAIT's is shown in Table 2 and in Fig. (11). For these calculations we assumed a discharge current of 10 A, a beam voltage of 1000 V, a current flux integral $C_j = 0.8$ and a grid open area fraction of 0.8. These values of C_j and ϕ_g are high, but probably achievable in a carefully designed engine. As noted above, this approach also neglects the power required for a neutralizer cathode, although this would be justified if a low power neutralizer such as a field emission array cathode were used with the ion source [?]. All of the performance parameters depend on the discharge current or beam voltage, so these results represent a point design which illustrates the impact of cathode material and the performance potential. The best materials appear to be chromium, copper, yttrium, gadolinium, tantalum and tungsten, with efficiencies of 0.42–0.64 and specific impulses at this beam voltage of 4030–7140 s. The impact of varying f_i or E_r to get a realistic upper bound on the ion mass fraction F_i is shown in Table (3). This reduces the specific impulse by 400–1500 s and the efficiency by 0.04–0.2. This suggests that the peak efficiencies for the best materials would be on the order of 0.45 for a beam voltage of 1000 V. The performance could, of course, be improved with higher beam voltages, as Fig. (12) shows. In this figure the total efficiency as

a function of specific impulse is plotted for the best cathode materials. The beam voltage ranges from 500 to 5000 V over these curves and for Cr, Gd , Ta and W the ion mass fraction F_i was assumed to be equal to one. As these curves show, the efficiency exceeds 0.5 at specific impulses of 3000 to 9000 s for the different materials. Because the ion generation occurs in a length scale on the order of 10 μm in the cathode spots, these results are largely independent of the engine size. This therefore appears to be an excellent approach for miniaturizing ion engines. The performance of conventional electron bombardment engines suffers as they are scaled to small sizes because the increased surface-to-volume ratio leads to less efficient plasma production [?].

Conclusions

The models described in this paper show how the performance of vacuum arc thrusters and vacuum arc ion engines scales with cathode material, engine geometry and operating parameters. These models were used with published values of material properties and optimistic estimates of parameters such as the ion current fraction and the current and momentum flux integrals to determine upper bounds on the performance potential of VAT's and VAIT's. The model results suggest that vacuum arc thruster configurations may be capable of operating at up to 9 percent total efficiency at a specific impulse of 900–1300 s. The advantages of this configuration are that it is very simple, requires no gas feed system, and can be operated with a very simple, low mass power processing unit [?]. The model shows that vacuum arc ion thrusters are capable of much higher performance because the ion acceleration is decoupled from the plasma production process. Efficiencies of 50–60 percent for specific impulses of 3000–9000 s should be achievable in carefully designed engines. This is a very exciting result, because this performance should be largely independent of engine scale. Very small, high performance VAIT's requiring no magnets and no gas feed systems and operating at very low average power levels (in low duty cycle pulsed operation) could be an ideal propulsion system for power- and mass-constrained microspacecraft.

Current work is focused on experimentally validating these models with direct thrust and electrical measurements and further characterizing the model input parameters. Preliminary thrust measurements for a VAT with a titanium cathode yielded a thrust-to-power ratio of 2.2 μN/W [?, ?]. Using the geometry of the thruster and the measured discharge voltage, the model described here predicts a performance of 3.5 μN/W. This is reasonably good agreement, given the uncertainties in the electrode geometry [?]. Additional thrust measurements using the thruster shown in Fig. (4) with different cathode materials, electrode geometries and discharge currents will be performed to further validate the model. Measurements of the electrical parameters and direct thrust measurements for the VAIT shown in Fig. (8) with various materials, geometries and operating conditions will be used to verify the VAIT model predictions. In addition, vacuum arc plasma sources are being characterized in a special ultra-high vacuum facility. The purpose of these experiments is to verify the model assumptions and measure the model input parameters such as erosion rates, ion current fractions, charge state distributions, angular ion current density distributions, ion velocities and discharge voltages [?].

Additional engineering challenges will have to be overcome to realize the potential of vacuum arc plasma sources. Arc ignition reliability with the triggerless method is an important issue, although preliminary tests demonstrating up to 1 million discharges are encouraging [?]. Uniform erosion of the cathode must be achieved and a reliable method of dispensing the consumable cathode must be developed. The threat of spacecraft contamination by condensible metal propellants has to be addressed. Finally, adequate engine lifetime must be demonstrated, which will require a thorough understanding of potential failure modes such as insulator and grid erosion and electrical shorts from metal vapor or macroparticle deposition. These are certainly challenging issues, but the predicted performance and scalability of vacuum arc-based thruster concepts indicate that the effort is justified. The unusual conditions achieved in vacuum arc discharges provide unique advantages for advanced propulsion systems.
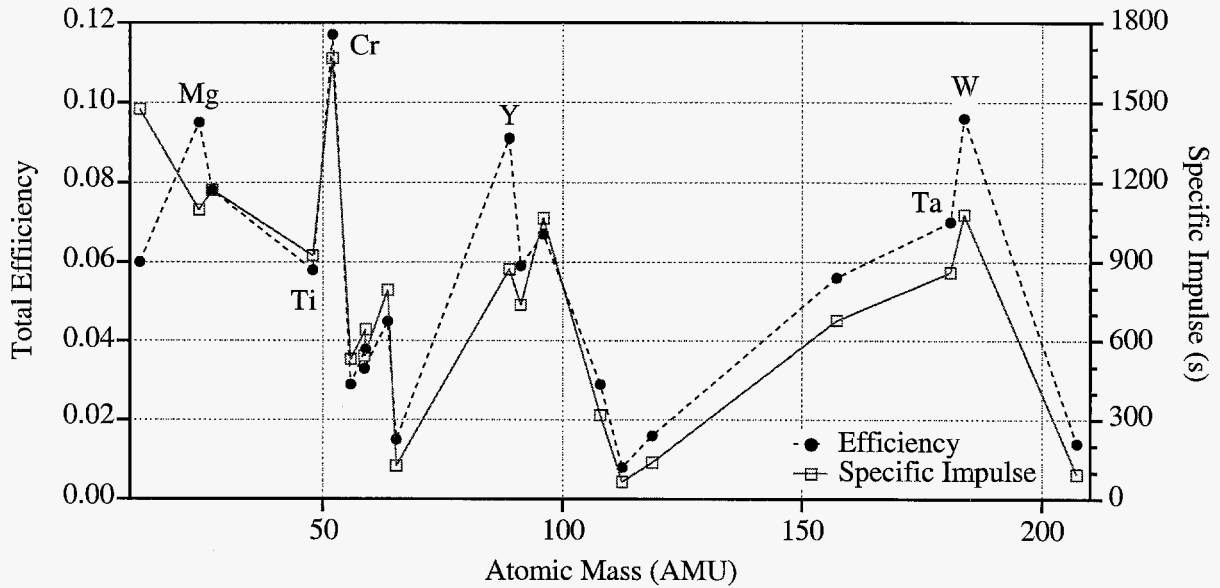
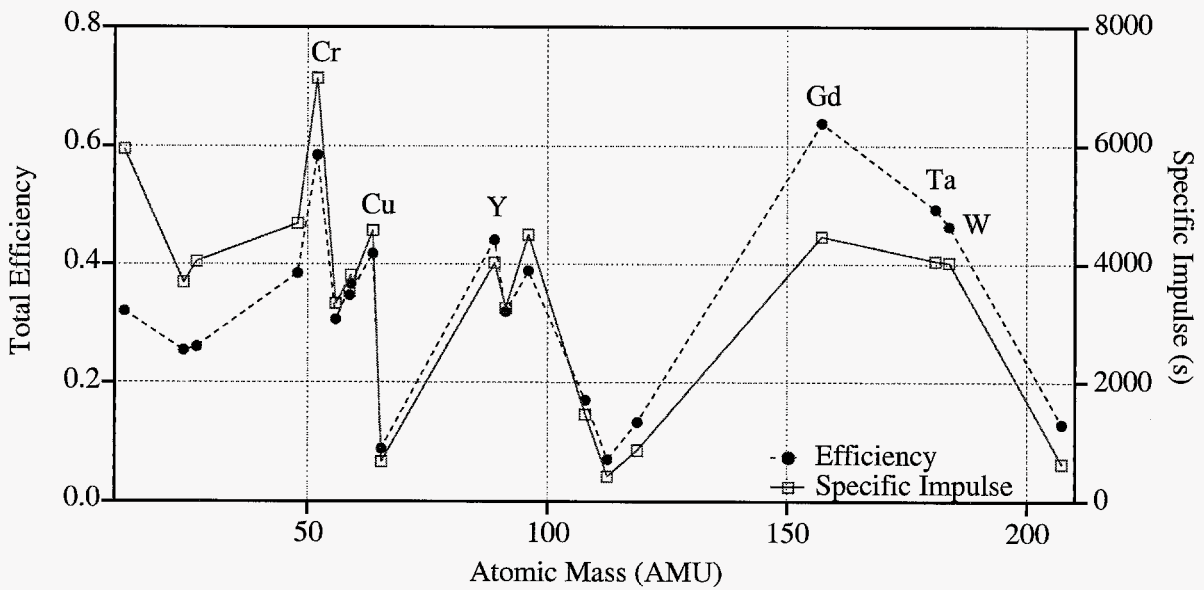Figure 10: Predicted performance of vacuum arc thrusters for various cathode materials.

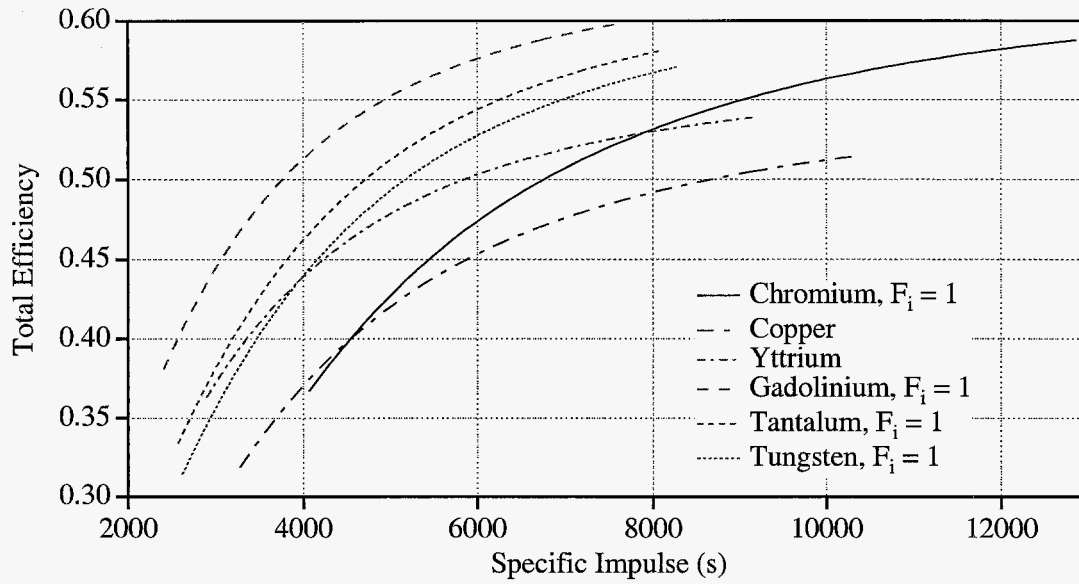Figure 11: Predicted performance of vacuum arc ion thrusters for various cathode materials.

Figure 12: Variation of VAIT efficiency with specific impulse for beam voltages ranging from 500 to 5000 V.

Species	Mass M_i (AMU)	Ion Charge State Distribution								Erosion Rate E_r (μg/C)	Ion Fraction F_i	Discharge Voltage V_d (V)	Ion Velocity u_i (m/s)
		f_1	f_2	f_3	f_4	f_5	f_6	$\langle Z^{-1}\rangle$	$\langle Z^{-1/2}\rangle$				
Li	6.941	1.000						1.00	1.00			23.5	23800
C	12	1.000						1.00	1.00	17	0.732	29.6	29700
Mg	24.305	0.307	0.701					0.66	0.80	31	0.528	18.8	30600
Al	26.981	0.224	0.590	0.191				0.58	0.75	28	0.577	23.6	29900
Si	28.086	0.450	0.504	0.043				0.72	0.83			27.5	25800
Ca	40.08	0.042	0.943	0.016				0.52	0.72			23.5	25900
Sc	44.96	0.150	0.749	0.101				0.56	0.74			19.1	
Ti	47.9	0.052	0.739	0.207				0.49	0.69	30	0.815	21.3	16700
V	50.94	0.038	0.664	0.280	0.019			0.47	0.68			22.5	19300
Cr	52	0.048	0.638	0.296	0.019			0.47	0.68	20	1.265	22.9	19400
Mn	54.94	0.327	0.658	0.020				0.66	0.80			22	10800
Fe	55.85	0.139	0.747	0.115				0.55	0.73	48	0.663	22.7	11800
Co	58.93	0.200	0.682	0.121				0.58	0.75	44	0.802	22.8	11800
Ni	58.71	0.167	0.727	0.102				0.56	0.74	47	0.736	20.5	10900
Cu	63.55	0.080	0.612	0.291	0.019			0.49	0.69	35	0.914	23.4	12800
Zn	65.38	0.667	0.333					0.83	0.90	320	0.176	15.5	10400
Ge	69.74	0.429	0.571					0.71	0.83			17.5	11000
Sr	87.62	0.010	0.990					0.50	0.71			18	
Y	88.91	0.022	0.544	0.434				0.44	0.66	45	0.898	18.1	14300
Zr	91.22	0.004	0.364	0.523	0.109			0.39	0.62	53	0.691	23.4	15700
Nb	92.91	0.003	0.160	0.510	0.293	0.033		0.33	0.57			27	15500
Mo	95.94	0.006	0.137	0.480	0.327	0.049		0.33	0.57	36	0.903	29.3	17400
Pd	106.4	0.121	0.713	0.144	0.021			0.53	0.72			21.3	15700
Ag	107.87	0.062	0.570	0.350	0.019			0.47	0.68	140	0.373	23.6	12500
Cd	112.41	0.523	0.485					0.77	0.87	620	0.142	16	6800
In	114.82	0.471	0.507					0.73	0.83			17.5	5500
Sn	118.69	0.313	0.693					0.66	0.80	295	0.273	17.5	7500
Ba	137.33	0.000	1.000					0.50	0.71			18.3	6700
La	138.91	0.005	0.685	0.311				0.45	0.67			17.2	7000
Ce	140.12	0.014	0.787	0.199				0.47	0.69			17.9	7000
Pr	140.91	0.014	0.613	0.373				0.44	0.66			20	8700
Nd	144.24		0.765	0.235				0.46	0.68			19.7	
Sm	150.4	0.010	0.779	0.211				0.47	0.68			14.6	7400
Gd	157.25	0.009	0.691	0.300				0.45	0.67	55	1.347	21.6	7400
Dy	162.5	0.009	0.574	0.417				0.43	0.66			19.8	7400
Ho	164.93	0.009	0.574	0.417				0.43	0.66			20	8300
Er	167.26	0.004	0.534	0.445	0.017			0.42	0.65			19	8200
Yb	173.04	0.014	0.867	0.118				0.49	0.70			14.4	
Hf	178.49	0.010	0.164	0.522	0.287	0.017		0.34	0.58			24.3	9200
Ta	180.95	0.007	0.225	0.389	0.328	0.051		0.34	0.58	56	1.143	28.7	11100
W	183.85	0.006	0.147	0.413	0.333	0.080	0.019	0.32	0.56	55	1.111	31.9	14300
Ir	192.22	0.019	0.278	0.519	0.165	0.019		0.38	0.61			24.5	
Pt	195.09	0.057	0.663	0.260	0.019			0.48	0.69			22.5	6800
Au	196.97	0.070	0.761	0.168				0.51	0.71			19.7	5800
Pb	207.2	0.225	0.780					0.62	0.78	510	0.257	15.5	5400
Bi	208.98	0.692	0.291					0.84	0.90			15.6	4200
Th	232.04	0.000	0.166	0.124	0.166			0.17	0.27			23.3	9900
U	231.04		0.075	0.547	0.377			0.31	0.56			23.5	11400

Table 1: Material and Arc Properties for Potential Cathode Materials

Species	Mass Flow Rate, $\dot{m}_t$ (mg/s)	Vacuum Arc Thruster				Vacuum Arc Ion Thruster					
		Thrust T (mN)	I_{sp} (s)	Total Efficiency η	Thrust-to-Power T/P (μN/W)	Thrust T (mN)	I_{sp} (s)	Propellant Efficiency η_u	Ion Production Cost ϵ_B (eV/ion)	Total Efficiency η	Thrust-to-Power T/P (μN/W)
Li		1.14			0.05	7.68			367		8.77
C	0.17	2.46	1475	0.060	0.08	10.09	5949	0.468	463	0.320	10.78
Mg	0.31	3.33	1096	0.095	17.73	11.42	3689	0.338	294	0.254	13.79
Al	0.28	3.20	1172	0.078	13.64	11.30	4044	0.370	369	0.260	12.90
Si		3.60			0.13	11.11			430		12.14
Ca		3.71			0.15	9.56			367		10.92
Sc						10.92			298		13.14
Ti	0.3	2.70	924	0.058	12.77	14.04	4689	0.522	333	0.385	16.46
V		3.17			0.13	9.72			352		11.24
Cr	0.2	3.27	1666	0.117	14.28	14.26	7143	0.810	358	0.585	16.41
Mn		2.69			0.12	14.21			344		16.52
Fe	0.48	2.50	531	0.029	11.01	15.95	3329	0.424	355	0.306	18.40
Co	0.44	2.77	643	0.038	12.17	16.75	3815	0.514	356	0.367	19.30
Ni	0.47	2.51	544	0.033	12.24	16.61	3540	0.471	320	0.347	19.65
Cu	0.35	2.73	794	0.045	11.65	15.98	4575	0.585	366	0.418	18.29
Zn	3.2	3.91	125	0.015	0.24	21.26	666	0.113	242	0.089	26.74
Ge		3.78			0.20	17.38			273		21.33
Sr						13.78			281		16.80
Y	0.45	3.85	872	0.091	21.27	18.06	4020	0.575	283	0.441	21.99
Zr	0.53	3.83	737	0.059	16.38	17.20	3251	0.443	366	0.319	19.68
Nb		3.31			0.12	9.36			422		10.29
Mo	0.36	3.77	1066	0.067	12.85	16.16	4498	0.578	458	0.389	17.32
Pd		6.13			0.28	15.99			333		18.74
Ag	1.4	4.30	317	0.029	0.18	20.45	1463	0.239	369	0.170	23.34
Cd	6.2	4.00	66	0.008	0.24	26.51	428	0.091	250	0.071	33.13
In		3.25			0.18	23.30			273		28.59
Sn	2.95	4.02	139	0.016	22.95	25.30	859	0.174	273	0.133	31.05
Ba		3.18			0.16	17.07			286		20.75
La		3.02			0.17	15.47			269		19.05
Ce		3.21			0.17	16.35			280		19.96
Pr		3.76			0.18	15.37			313		18.30
Nd						16.13			308		19.27
Sm		3.61			0.23	16.78			228		21.35
Gd	0.55	3.65	677	0.056	16.90	24.51	4466	0.862	338	0.638	28.64
Dy		3.61			0.17	16.15			309		19.27
Ho		4.11			0.20	16.27			313		19.37
Er		4.01			0.20	15.97			297		19.24
Yb						18.69			225		23.84
Hf		3.87			0.15	13.29			380		15.05
Ta	0.56	4.70	861	0.070	16.49	22.64	4050	0.732	448	0.493	24.42
W	0.55	5.80	1078	0.096	18.24	22.12	4029	0.711	498	0.464	23.06
Ir						15.19			383		17.16
Pt		4.40			0.19	19.57			352		22.62
Au		4.00			0.19	20.76			308		24.80
Pb	5.1	4.71	94	0.014	30.39	32.36	636	0.164	242	0.129	40.70
Bi		5.18			0.31	36.00			244		45.23
Th		2.62			0.11	7.35			364		8.42
U		5.72			0.23	13.93			367		15.92

Table 2: Predicted Performance of Vacuum Arc Thrusters and Vacuum Arc Ion Thrusters

Species	Erosion Rate, E_r (μg/C)	Ion Current Fraction f_i	Ion Mass Fraction F_i	Vacuum Arc Thruster			Vacuum Arc Ion Thruster			
				I_{sp} (s)	Total Effici-ency η	Thrust-to-Power T/P (μN/W)	I_{sp} (s)	Propellant Efficiency η_u	Total Effici-ency η	Thrust-to-Power T/P (μN/W)
Cr	20	0.100	1.265	1666	0.117	14.3	7143	0.81	0.585	16.4
	20	0.079	1.000	1316	0.073	11.3	5643	0.64	0.432	15.3
	25.3	0.100	1.000	1317	0.092	14.3	5647	0.64	0.462	16.4
Gd	55	0.100	1.347	677	0.056	16.9	4464	0.86	0.638	28.6
	55	0.074	1.000	501	0.031	12.5	3304	0.64	0.434	26.3
	74	0.100	1.000	503	0.042	16.9	3319	0.64	0.474	28.6
Ta	56	0.100	1.143	861	0.070	16.5	4050	0.73	0.493	24.4
	56	0.087	1.000	749	0.053	14.4	3523	0.64	0.410	23.3
	64	0.100	1.000	754	0.061	16.5	3544	0.64	0.432	24.4
W	55	0.100	1.111	1078	0.096	18.2	4029	0.71	0.464	23.1
	55	0.090	1.000	970	0.078	16.4	3626	0.64	0.402	22.2
	61	0.100	1.000	972	0.087	18.2	3632	0.64	0.418	23.1

Table 3: Effect of decreased ion mass fraction or increased erosion rate on performance.